DEPENDENCE OF THE ASYMMETRY ENERGY AND TIME IN DYNAMICAL MODELS USING ISOSCALING

A Thesis

by

ANDREW C. RAPHELT

Submitted to the Office of Graduate and Professional Studies of
Texas A&M University
in partial fulfillment of the requirements for the degree of

MASTER OF SCIENCE

Chair of Committee,	Sherry J. Yennello
Committee Members,	Joseph B. Natowitz
	Che-Ming Ko
	Charles M. Folden III
Head of Department,	David H. Russell

May 2014

Major Subject: Chemistry

ABSTRACT

The asymmetry energy (E_{sym}) term of the equation of state for nuclear matter has been studied using fragment distributions and isoscaling. Reactions of ^{64}Ni+^{64}Ni, ^{64}Zn+^{64}Zn, and ^{70}Zn+^{70}Zn were investigated at the Texas A&M University Cyclotron Institute using the NIMROD-ISiS array to collect the data. The same reactions were simulated using anti-symmetrized molecular dynamics (AMD), constrained molecular dynamics (CoMD), and GEMINI, a statistical decay model, used as an afterburner for the dynamical models. The dynamical models were studied at time-steps, or maximum times, of 300 fm/c and 3000 fm/c. In the AMD simulations, GEMINI was applied at 300 fm/c to de-excite the system. The fragment distributions and isoscaling exhibit a dependence on the time-step of the simulation, due to the differences in de-excitation of the system, as well as the E_{sym} of the interactions in AMD and CoMD.

Charge and mass distributions, isotope distributions, and multiplicity distributions were analyzed for the AMD and CoMD simulations and experimental data. The fragment distributions showed a dependence on the time-step of the simulation as well as the E_{sym} of the simulations. The isoscaling also exhibited both time and E_{sym} dependence in the simulations. The dependence on isoscaling with time is not affected by the use of GEMINI as an afterburner, as compared to allowing the system to de-excite dynamically.

Quasi-projectiles (QP) were reconstructed from the simulations and experimental data. The fragments from the QP were studied using the same fragment distributions and isoscaling as in the inclusive data. The fragment distributions were less affected by the time-step of the simulation compared to the fragments before reconstruction, and did not show a large dependence on E_{sym}. The QP isoscaling exhibited an E_{sym} dependence and a time-step dependence. The isoscaling results for the AMD simulations are not affected by a dynamical de-excitation compared to a statistical de-excitation.

In the isoscaling analysis, the experimental data agree well with the simulations at later time-steps. The agreement of the simulations with the experimental data is not dependent on the use of a dynamical or statistical model to de-excite the system. The experimental data and simulations in this work are also compared with previous work and the results and conclusions are consistent with the previous results.

To my wife Donna

ACKNOWLEDGEMENTS

I would like to thank my committee chair, Dr. Sherry Yennello, for her guidance and support throughout the course of this research and for her immeasurable amounts of advice in school and life. I would also like to thank my committee members, Dr. Joseph B. Natowitz, Dr. Che-Ming Ko, and Dr. Charles M Folden III. I would like to thank all of the graduate students, post-docs, and undergraduates who have always been willing to help and encourage me during graduate school. I would like to specially thank Dr. Zach Kohley for his work and his assistance in using his experimental data and the AMD and CoMD simulations. I would also like to thank Dr. Aldo Bonasera and Dr. George Souliotis for their helpful discussions. I would like to thank all of the staff members at the Texas A&M University Cyclotron Institute and Chemistry Department who have helped me throughout graduate school. I would like to thank the Department of Energy for support of this research through grant number DE-FG03-93ER40773 and the Robert A. Welch Foundation through grant number A-1266.

I would like to thank my family for their encouragement during graduate school and their continued support. Finally, I would like to thank my wife, Donna, who has always encouraged me in everything I have done and has offered me an immense amount of support and love.

TABLE OF CONTENTS

Page

LIST OF FIGURES

LIST OF TABLES

CHAPTER I

INTRODUCTION

The equation of state (EoS) of nuclear matter is an important topic in the field of nuclear science and governs the behavior of nuclear reactions. Constraining the EoS can provide a better understanding of nuclear reactions. Nuclear reaction simulations and models produce many forms of the EoS which can be studied by analyzing fragment distributions and isoscaling. Analyzing the results from simulations and comparing them to experimental results can lead to better constraints of the EoS by showing how systems de-excite and fragment and how a reaction changes over the course of time.

1.1 Equation of State

The nuclear equation of state (EoS) describes the relationship of various thermodynamic states and properties in nuclear matter. The EoS relates properties such as temperature, density, and pressure. The EoS, and specifically the asymmetry energy term in the EoS, is important for determination of neutron skin thickness and nuclear structure at the drip line [1].

For ground state nuclei, the temperature and density are well defined, where T=0 MeV and ρ_0=0.16 nucleons/fm^3. The binding energy for ground state nuclei is described by the liquid drop model, developed by Weizsäcker [2]. The liquid drop model, or Weizsäcker mass formula, is:

$$E_B = a_V A - a_S A^{2/3} - a_C \frac{Z^2}{A^{1/3}} - a_{sym} \frac{(N-Z)^2}{A} \pm \delta \tag{1.1}$$

where the binding energy, E_B, depends on the charge (Z) and mass (A) of the system, as well as the coefficients for the volume (a_v), surface (a_s), Coulomb (a_c), asymmetry (a_{sym}), and pairing (δ). The asymmetry coefficient is well-constrained near the ground state, but is not well-defined at densities, temperatures, and neutron-to-proton (N/Z) ratios away from the ground state.

The EoS, in relation of the asymmetry term, can be expressed in the parabolic form:

$$\frac{E(\rho,I)}{A} = \frac{E}{A}(\rho,0) + \frac{E_{sym}}{A}(\rho)I^2 \qquad , \qquad I = \frac{\rho_n-\rho_p}{\rho_{Total}} \approx \frac{N-Z}{A} \tag{1.2}$$

where E(ρ,I)/A is the binding energy as a function of the density, ρ, and the isospin concentration, I [3]. The isospin concentration is the difference between the density of the neutrons and the density of the protons, which, in finite systems, can be approximated as the difference between the number of neutrons and the number of protons. The first term in the EoS represents the energy per nucleon as a function of density for symmetric nuclear matter, where I=0. The second term represents the energy per nucleon of asymmetric nuclear matter as a function of density and isospin, where the isospin dependence is I^2. The asymmetry energy, E_{sym}, is related to the a_{sym} term from the binding energy equation and can be thought of as the energy required to convert all protons into neutrons in symmetric nuclear matter [4]. The energy per nucleon from the EoS is plotted against the reduced density in Figure 1, to show the density dependence of the energy in the EoS.

The energy per nucleon for infinite symmetric nuclear matter and infinite pure neutron matter are shown in Figure 1. The nuclear matter curves are for infinite symmetric nuclear matter (I=0), and the neutron matter curves are for infinite pure neutron matter (I=1). The various forms of the EoS are often described by the the curvature of the EoS around the saturation density, represented by the compressibility, K, [5] where:

$$K = 9\rho_0^2 \frac{d^2(E/A)}{d\rho^2}\bigg|_{\rho_0} \quad . \tag{1.3}$$

Previous constraints on the compressibility of symmetric nuclear matter have been studied and the compressibility is considered to be around K=220-270 MeV [6]. The forms of the EoS are often termed as “stiff” or “soft”, depending on the magnitude of the compressibility, with higher values around 300 MeV considered “stiff” and lower values around 200 MeV considered “soft” [5]. The stiff interactions have a larger curvature in Figure 1, while the soft interactions have a smaller curvature. At the saturation density, the compressibility is well defined and the various forms of the EoS agree reasonably well, but away from the saturation density, the various models in Figure 1 differ greatly.

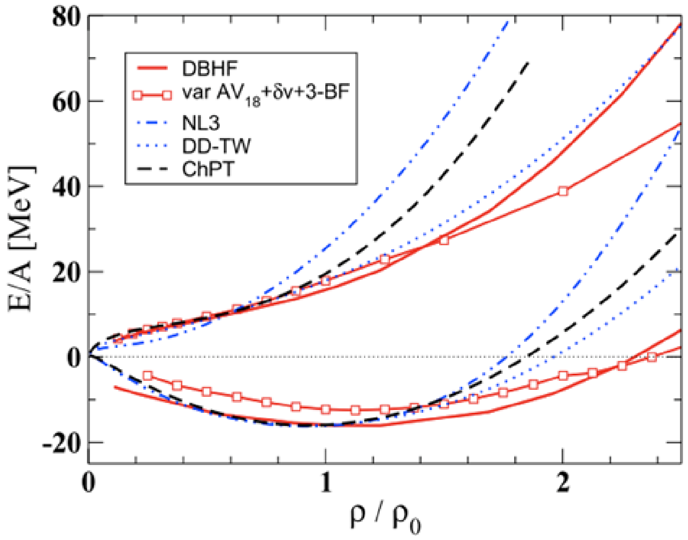

Figure 1. Energy per nucleon vs. the reduced density, ρ/ρ_o, from the EoS, for infinite symmetric nuclear matter (bottom curves) and pure neutron matter (top curves) adapted from [5].

The asymmetry energy, the second term in Eq 1.2, describes the energy for asymmetric nuclear matter. The asymmetry energy is the difference in the energy per nucleon of the pure neutron matter minus the symmetric nuclear matter shown in Figure 1. The density dependence of E_{sym} shows how E_{sym} behaves over a range of densities. Different interactions from the models shown in Figure 1 give varying approximations of E_{sym} at densities away from normal nuclear density. Many of these interactions still agree near normal nuclear density.

The curvatures of the interactions in Figure 2 are described as asy-soft and asy-stiff, similar to the descriptions of the curvature of the equation of state in Figure 1. Asy-soft interactions bend over at high density, while the asy-stiff interactions increase at higher density. For the rest of this work, the terms “soft” and “stiff” will be used in reference to “asy-soft” and “asy-stiff” asymmetry energy curves.

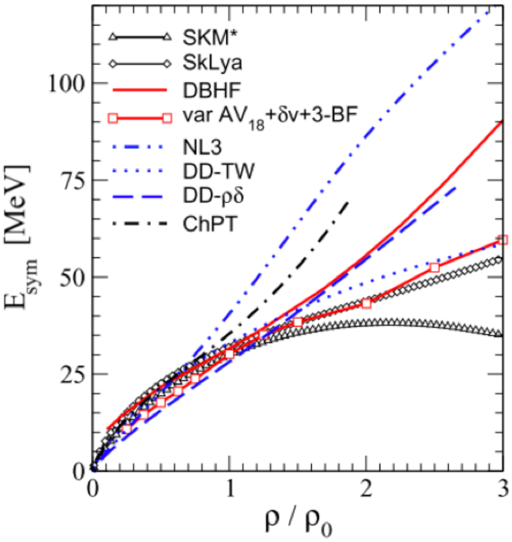

Figure 2. Plot of the asymmetry energy, E_{sym}, vs. the reduced density, ρ/ρ_0 adapted from [5].

1.2 Simulations

Many theoretical models describe nuclear reaction mechanisms at and away from saturation density. Most models agree on the value of E_{sym} at saturation density, but away from saturation density, the models deviate from each other. There are multiple types of models and each treat nuclear reactions in different ways. Each model begins with a set of assumptions and physical parameters and predicts what will happen based on these parameters.

Dynamical models, such as anti-symmetrized molecular dynamics (AMD) [7], constrained molecular dynamics (CoMD) [8,9] (classical molecular dynamics (CMD) [10], and stochastic mean field (SMF) [11] follow the nuclear reaction as it progresses in time. The dynamical models allow for the observation and analysis of fragments at early time-steps, during the collision, and at later time-steps, after the system has cooled. Statistical models, such as GEMINI [12] and the statistical multifragmentation model (SMM) [13] start with an excited system and de-excite the reaction using sequential or simultaneous decay to produce fragments. The statistical model is used to de-excite the system from an early time-step to produce cooled secondary fragments [14]. For both dynamical and statistical models, the fragmentation and de-excitation is based on the EoS of the model and the excitation energy, density, size, N/Z, and angular momentum of the system.

This study will compare two dynamical models, AMD and CoMD, as well as one statistical model, GEMINI, to analyze their fragment production in comparison to experimental data. The fragments produced by the different types of dynamical and statistical models can vary in N/Z composition, multiplicity, and excitation energy due to how the model simulates the nuclear reaction. AMD and CoMD use several forms of E_{sym}, which range from asy-soft to asy-stiff. Figure 3 shows the density dependence of the asymmetry energy for the five interactions from the two models.

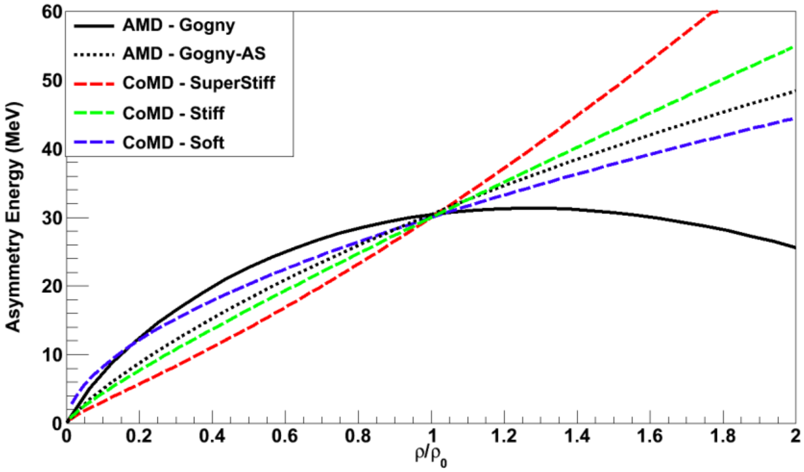

Figure 3. Asymmetry energy vs. reduced density for AMD and CoMD simulations

The AMD model can be run with either of two interactions, the soft Gogny interaction, or the stiff Gogny-AS interaction, while the CoMD model has three interactions, the Soft, Stiff, and Super-Stiff. These different asymmetry energy potentials affect the fragmentation of the system. The two dynamical models, AMD and CoMD, along with the statistical model, GEMINI, provide a large variation in fragment production. These models will affect the production of fragments with various N/Z, multiplicity, and isotopes due to the differences in the models as well as the differences in the asymmetry energies in each model.

1.3 Fragment Distributions

Each simulation produces a variety of different types of fragments based on the parameters of the model. Some ways to analyze these fragments are by looking at the fragment multiplicity, isotope distributions, and charge and mass distributions. Each of these distributions is affected by the N/Z of the system and the excitation energy as well as what model and E_{sym} are being used. The fragment multiplicity distribution shows how many fragments result from the breakup of the system. In general, at higher excitation energy the system will break up into more fragments than at lower excitation energy.

Charge and mass distributions are created from the isotope produced in the reaction. Similar to the fragment multiplicity distribution, the excitation energy in the system affects the charge and mass distribution. Higher excitation energy events will produce a high multiplicity, which corresponds to a lower peak in the charge and mass distribution, due to the charge and mass of the system being distributed amongst the fragments. The opposite is true for lower excitation energy events, where the charge and mass distributions will be peaked higher due to less fragmentation.

The yield of the isotopes produced in a nuclear reaction depends on the N/Z of the system as well as the asymmetry energy. The asymmetry energy governs the neutron-richness of fragments produced by the simulation, and can affect which isotopes are more abundantly produced for each element. Protons and neutrons behave differently in stiff and soft interactions, and this behavior affects the isotope distributions for each of the elements [3]. An example of this behavior is shown by neutrons, which have a larger repulsion at softer asymmetry energies than at stiffer asymmetry energies [3]. Using a statistical model to de-excite the system also influences the isotopic distributions, as the system undergoes additional fragmentation with the inclusion of a statistical model [7].

Figure 4 shows the effect of secondary decay on isotope production from simulations in comparison to experimental data [15]. The primary fragments from AMD simulations of $^{12}C+^{12}C$ at 28.7 MeV/nucleon at 200 fm/c. The secondary fragments are produced by the use of CASCADE as an afterburner to the AMD at 200 fm/c. At 200 fm/c, the fragments from AMD still have some excitation energy and can be considered "hot" fragments. When the afterburner is applied to the system at 200 fm/c, the excited

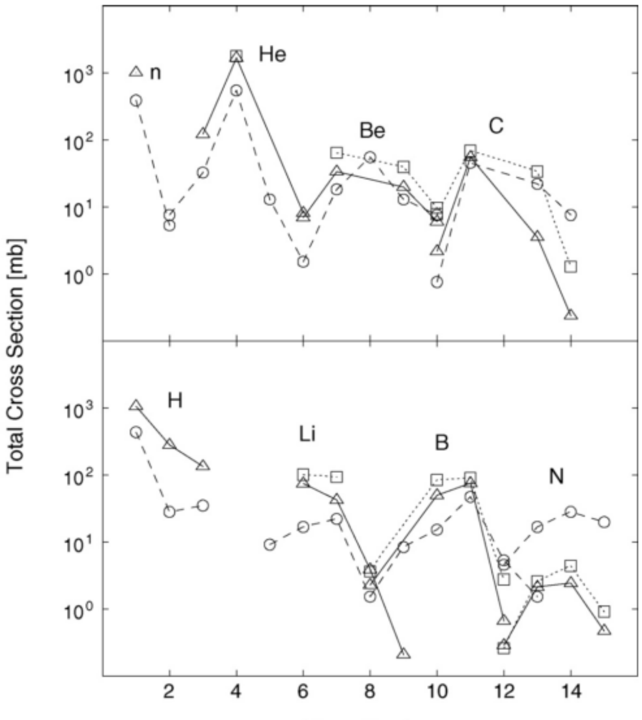

Figure 4. Isotope distributions for primary fragments from AMD (circles), after secondary decay by CASCADE (triangles), and experimental data (squares) for $^{12}C+^{12}C$ at 28.7 MeV/nucleon adapted from [15].

fragments de-excite by additional fragmentation and particle emission until the system is considered "cool" and there is no excitation energy left in the system. For the isotope distributions, the experimental data does not agree exactly with the primary or secondary fragments for all of the elements. For most of the elements, the cross section of the secondary fragments shows a closer agreement to the results from the experiment, but the carbon isotope distribution from the experimental data has a closer cross section to the primary fragments. Figure 4 displays the change in the results of the simulation at early and later stages of the reaction, and a comparison to experimental data.

By using each of these fragment distributions, comparisons can be drawn between experimental data and the E_{sym} of various models. The distributions show not only which model and E_{sym} more closely matches the data, but also a difference between the dynamical and statistical models. The effect of the asymmetry energy and interaction, as well as the study of primary and secondary fragments, provides several ways to compare simulations to experimental data.

1.4 Isoscaling

Looking at detailed distributions provides a comparison of one observable of a reaction, such as mass, charge, or multiplicity. Scaling the data allows us to look at the reaction in a more global way. Isoscaling [16] relates the isotope yields measured in two different nuclear reactions, such that:

$$\mathrm{R}_{21}(\mathrm{N},\mathrm{Z}) = \frac{\mathrm{Y}_2(\mathrm{N},\mathrm{Z})}{\mathrm{Y}_1(\mathrm{N},\mathrm{Z})} \tag{1.4}$$

where $R_{21}(N,Z)$ is the ratio of the isotope yields of fragments from the neutron-rich reaction $Y_2(N,Z)$ to those from the neutron-poor reaction $Y_1(N,Z)$. This ratio has also been shown to follow an exponential dependence [17] where:

$$R_{21}(N,Z) = Ce^{(\alpha N+\beta Z)} \tag{1.5}$$

In this expression, the isotope yield ratio is related to the differences between the chemical potentials of the neutrons, $\alpha=\Delta\mu_n/T$, and the protons, $\beta=\Delta\mu_p/T$, in the two systems, and C is a normalization constant. The scaling relationship can be visualized by plotting the ratio versus the number of neutrons in each isotope.

Figure 5 plots the fragments emitted in reactions of ^{60}Ca+^{60}Ca vs. ^{40}Ca+^{40}Ca relative to the number of neutrons in each isotope for AMD Gogny and Gogny-AS simulations at 300 fm/c. The ratios are plotted on an exponential scale and the isotopes for each element are fit using a linear fit. The open and filled squares alternate for each element to distinguish between the elements. When plotted in this manner, the slope of the line fit to each element is the α value from Eq. 1.5. In this figure, one α value has been extracted from a global fit of all of the elements at once, which allows the isoscaling of this reaction to be defined by a single α value for all elements, instead of an

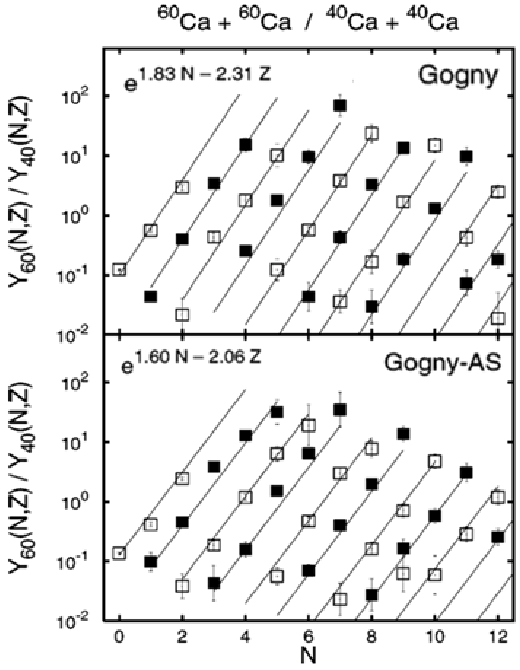

Figure 5. Isoscaling of ^{60}Ca+^{60}Ca/^{40}Ca+^{40}Ca at 35 MeV/nucleon from AMD simulations at 300 fm/c. α and β from Eq 1.5 are shown at the top left of the figure adapted from [18].

α value for each element. The β value can also be extracted from the fit of Eq 1.5 to the data in this figure. The β value is negative and can be visualized as the slopes of the fits if the ratio is plotted against the number of protons instead of the number of neutrons. In Figure 5, the magnitude of β is the distance between the lines for each element.

The isoscaling parameter, α, has been shown to be linked to E_{sym} [17] through the equation:

$$\alpha=\frac{4C_{sym}}{T}\left[\left(\frac{Z_1}{A_1}\right)^2-\left(\frac{Z_2}{A_2}\right)^2\right]=\frac{4C_{sym}}{T}\Delta \qquad (1.6)$$

where C_{sym} is the asymmetry energy, T is the temperature, and Δ is the difference in the proton-to-mass ratio between the two systems used in the ratio, where $(Z/A)_1$ is the ratio from the neutron-poor system, and $(Z/A)_2$ is the ratio from the neutron-rich system. This expression provides a path to extract an E_{sym} value from the isoscaling analysis, for systems with a known temperature. This equation also shows the effect of the fragment asymmetry, Δ, on the isoscaling parameter, α. A greater difference in the asymmetry between the two systems corresponds to a larger α value.

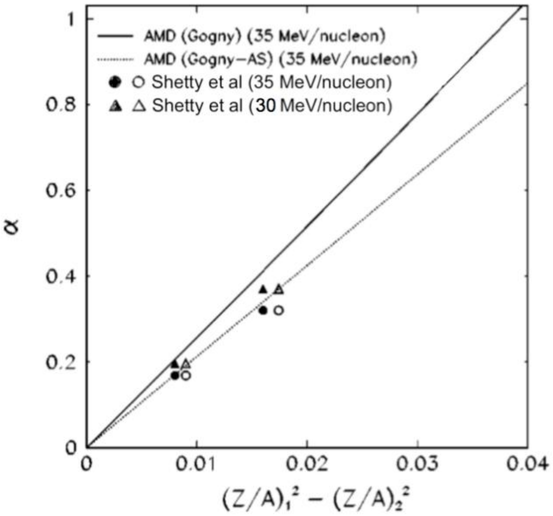

Figure 6. Isoscaling parameter α as a function of the asymmetry of the fragments, Δ. The lines are from AMD calculations at 300 fm/c and the points are various experimental results adapted from [20].

The dependence of α on Δ can be seen by plotting α vs. Δ [20] as shown in Figure 6. In Figure 6, the isoscaling parameter, α, from various reactions is plotted against the fragment asymmetry from the reaction. This figure contains results of isoscaling from AMD Gogny and Gogny-AS simulations at 300 fm/c as well as results from isoscaling of experimental data. The lines for the AMD data are fits to the α and Δ values from reactions of ^{40}Ca+^{40}Ca, ^{48}Ca+^{48}Ca, and ^{60}Ca+^{60}Ca at 35 MeV/nucleon, using central collisions and only A>4 fragments in the Δ calculation [18]. The experimental results are from reactions of ^{58}Fe+^{58}Fe, ^{58}Fe+^{58}Ni, and ^{58}Ni+^{58}Ni at 30, 40, and 47 MeV/nucleon detected in a silicon telescope at θ_{lab}=44° [20]. The α value is extracted from isoscaling plots only using fragments with a charge of $3 \leq Z \leq 7$, and the Δ value is extrapolated from comparison to AMD simulations at 300 fm/c [20]. The silicon telescope at 44° and selection of fragments with a charge of $3 \leq Z \leq 7$ selects on mostly central collisions and allows for a fair comparison to the AMD simulation. Figure 6 shows the linear relationship between the isoscaling parameter, α, and fragment asymmetry, Δ, from Equation 6. From this figure, the globally extracted isoscaling parameter α from experimental data plotted as a function of Δ appears to correspond more with the stiff Gogny-AS form of AMD, instead of the soft Gogny form. However, this has only taken into account a dynamical model at a short time scale, and does not include statistical decay or a long timescale for secondary decay of the system.

Isoscaling has been shown to hold true for various reactions involving both multifragmentation at higher energies [21] and heavy residues at lower energies [22] as well as results from dynamical models [18] and statistical models [17].

1.5 Quasi-Projectile Reconstruction

The isoscaling analysis in the previous section uses all of the fragments from the reactions in the analysis. Recently, isoscaling has also been studied using only fragments emitted from a reconstructed quasi-projectile (QP), instead of the entire system [19]. Reconstructed quasi-projectiles have been shown to improve the isoscaling relation due to a more accurate knowledge of Δ [19]. During mid-peripheral nuclear reactions, where the target and projectile overlap during the collision, a QP can be formed from the projectile fragment after the reaction. The QP is generally the same size or slightly smaller than the projectile and contains nucleons from the projectile as well as some nucleons from the target that were exchanged while the projectile was in contact with the target. The QP is formed immediately after the collision of the projectile and target and is excited due to the exchange of nucleons between the projectile and target. The excited QP will then undergo fragmentation and particle emission in order to de-excite. The fragments that are emitted from the QP can be detected in a detector array and from these fragments, the QP can be reconstructed [19]. The reconstruction of the QP produces a roughly spherical source from which fragments are emitted isotropically in the QP frame. Cuts are made to the QP sources from the data to isolate specifically equilibrated, spherical QP sources to analyze. This QP selection allows for analysis of a statistical type of reaction from experimental data.

From the newly reconstructed QP, fragment distributions can be observed using only particles that are present in a QP. When studying reactions without a reconstructed QP, the source is defined as the detected fragments that make it through the event selection. Using an equilibrated, spherical QP source for isoscaling, instead of the total reaction system, improves the isoscaling because the definition of the source is improved as shown in Figure 7 [19].

In Figure 7, the top plot shows isoscaling from fragments detected in the NIMROD-ISiS array from reaction of ^{86}Kr+^{64}Ni/^{78}Kr+^{58}Ni. The bottom shows isoscaling of fragments emitted from reconstructed QP for reactions of ^{86,78}Kr+^{64,58}Ni. The values of the isoscaling fits for each element from fragments from reconstructed QP sources are much closer to each other than the values of the fits for fragments before the reconstruction. The QP reconstruction improves the values that can be extracted from the isoscaling, by producing similar α values for every element in the isoscaling, and allows for the better definition of a global α parameter to define the isoscaling of the entire system. Using the improved isoscaling results, the isoscaling parameter α can be

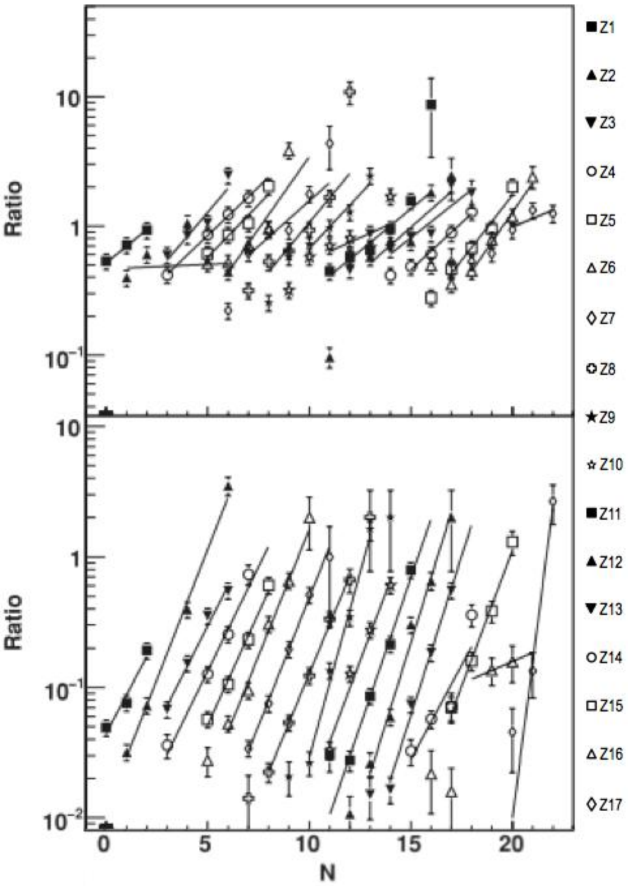

Figure 7. (Top) Isoscaling of ^{86}Kr+^{64}Ni/^{78}Kr+^{58}Ni at 35 MeV per nucleon using the 4π NIMROD-ISiS array. (Bottom) Isoscaling of ^{86,78}Kr+^{64,58}Ni using reconstructed QP sources adapted from[19].

studied with its relation to Δ both from experimental data and by implementing the QP reconstruction on simulated data. The charge, mass, isotopic, and N/Z ratios can also be studied in relation to how the QP reconstruction of experimental and simulated data affect them.

1.6 Proposal

Understanding the EoS and the E_{sym} term is important to describe nuclear reaction mechanisms. Theoretical models provide several types of interactions that produce various results. Dynamical models provide the possibility to observe the system at multiple time-steps to study the reaction at different stages of fragmentation. In this work, several time-steps, the maximum time that the simulation was run to, will be studied. Simulations using the dynamical models AMD and CoMD will be studied using reactions of ^{64}Ni+^{64}Ni, ^{64}Zn+^{64}Zn, and ^{70}Zn+^{70}Zn to time-steps of 300 fm/c and 3000 fm/c. The statistical model GEMINI will also be applied to the simulations at short time-steps of 300 fm/c and 3000 fm/c. Comparing experimental data of the same reaction systems to the data from the models can show which interaction from each model matches most closely to experimental results and how the time-step of the dynamical model affects different observables and their agreement with the experiment. Statistical models may also show an effect in the analysis when used to de-excite fragments from dynamical models, rather than allowing them to be de-excited dynamically. These comparisons between the simulations and experiment can be observed using fragment distributions, such as charge and mass distributions, multiplicity distributions, and isotope distributions, as well as by using isoscaling. Adding a QP reconstruction to previously performed analyses provides the ability to analyze a unique source, and may also provide insight on how the simulations and experiment compare. The various forms of the E_{sym} from the models, as well as the difference in dynamical and statistical models can provide many comparisons to the experimental data.

CHAPTER II

SIMULATIONS

Results from several theoretical models, both dynamical and statistical, were compared to experimental data. Below is a discussion of the dynamical and statistical models used in this work, as well as the experimental setup.

2.1 Dynamical Models

Dynamical simulations model the interaction of nuclei in a collision with respect to time. Time-dependent wave-functions are calculated for each nucleus in the system at multiple time-steps. In this work, two dynamical simulations are used to model the reactions: the momentum-dependent anti-symmetrized molecular dynamics (AMD) and the momentum-independent constrained molecular dynamics (CoMD).

2.2 Anti-Symmetrized Molecular Dynamics (AMD)

The anti-symmetrized molecular dynamics model is characterized by its use of the Slater determinant to describe the wave-function of nuclei. The Slater determinant wave-function, $\Phi(Z)$,can be expressed as [23]:

$$\Phi(\mathrm{Z}) = \det\left[\exp\left\{-\nu\left(\mathbf{r}_j - \frac{\mathrm{Z}_i}{\sqrt{\nu}}\right)^2 + \frac{1}{2}\mathbf{Z}_i^2\right\}\chi_{\alpha_i}(j)\right] \tag{2.1}$$

The complex variables, Z≡ $\{Z_i;i=1,\ldots,A\}=\{Z_{i\sigma};i=1,\ldots,A,\sigma=x,y,z\}$, represent the centroids of the wave packets used in the wave-function. The spin and isospin states of p↑, p↓, n↑, n↓ are represented by the variable χ_{α_i} [23]. The wave packet centroid, Z_i, is defined as [23]:

$$\mathbf{Z}_i = \sqrt{\nu}\mathbf{D}_i + \frac{i}{2h\sqrt{\nu}}\mathbf{K}_i \tag{2.2}$$

where the width parameter, $\nu=0.16\text{fm}^{-2}$, is constant for all wave packets, and D_i and K_i represent the centroids of the position and momentum respectively for each nucleon [7].

The time evolution of the wave packet centroid, Z, is determined by the time-dependent variation principle, which provides an equation of motion for the centroids D_i and K_i. These position and momentum centroids lose physical meaning in the nucleus due to anti-symmetrization in the AMD model [23].

Since the centroids of the position and momentum for each nucleon do not have physical meaning in the definition of Z, the physical coordinate $W \equiv \{W_i; i=1,\ldots,A\} = \{W_{i\sigma}; i=1,\ldots,A, \sigma=x,y,z\}$ is introduced which is defined as [23]:

$$\mathbf{W}_i = \sum_{j=1}^{A} \left(\sqrt{Q_{ij}}\right) \mathbf{Z}_i \tag{2.3}$$

so that the physical coordinate, W, is derived from the complex variable, Z. Using the physical coordinate, W, makes it possible to study two-nucleon collisions, which cannot be done with the complex variable Z. To take into account the fermionic nature of the nucleons, also known as the Pauli principle, the Slater determinant is used to represent the system. In a nuclear collision, the W for each nucleon cannot get within a set distance of each other due to Pauli blocking. When there is Pauli blocking in a nuclear collision, the coordinate, W, has no Z that will satisfy Eq. 2.3. When W is not in a Pauli blocking region, a solution for Z can be found to satisfy W [7].

An important part of most nuclear reaction simulations is the inclusion a stochastic term to allow a single initial state to fragment into a variety of final states. In the AMD model, the fragmentation has been extended to include quantum branching of the initial state into a distribution of final states, which exceeds the effects of simple stochastic nucleon-nucleon collisions. The quantum branching is accomplished by propagating the Gaussian wave packets by the Vlasov equation, which represents single-particle motion in a mean field. After some time, τ, decoherence into AMD wave packets takes place as the system fragments and undergoes stochastic quantum branching. AMD-V (for Vlasov), also called AMD-D (for diffusion), also takes into consideration the branching from the wave packet diffusion effect in the mean field propagation. When a finite coherence time, τ, is introduced, instead of the τ used in the original AMD, a wave packet shrinking effect in the mean field propagation is also observed in the dynamics. This model is now called AMD-DS since it includes both the diffusion and the shrinking. The added shrinking in AMD-DS creates a slower expansion after the collision, compared to AMD-D, which increases production of heavier fragments and shows improved agreement with experimental results.

The AMD-DS model was used in this work and the analyzed results are used to compare to experimental data. Simulations were analyzed at 300 fm/c to observe the fragments immediately after fragmentation. These fragments are still excited, or hot, and can be de-excited in multiple ways. The hot fragments can be de-excited by using the statistical decay code GEMINI, or the simulation can be extended to a time of 3000 fm/c to allow the fragments to cool dynamically. The AMD Gogny and Gogny-AS interactions in this work are analyzed at time-steps of 300 fm/c, 3000 fm/c, and 300 fm/c with GEMINI.

The momentum-dependent Gogny and Gogny-AS interactions were used in the AMD-DS simulations. The two interactions have different compressibilities, as defined by Eq. 1.3, which are dependent on the asymmetry energy from the equation of state. The Gogny interaction has a compressibility of K_{asy}=228 MeV [23] while the Gogny-AS interaction has a compressiblity of K_{asy}=360 MeV [7]. These compressibilities correspond to a Gogny interaction with an asy-soft density dependence of the asymmetry energy, and a Gogny-AS interaction with an asy-stiff dependence of the asymmetry energy. The results from the simulations of the two interactions can be compared to the experimental data to see how the experimental data compares to each asymmetry energy.

2.3 Constrained Molecular Dynamics (CoMD)

The constrained molecular dynamics (CoMD) model introduces the concept of constraint to molecular dynamics. One of the main differences between the CoMD model and the AMD model is the description of the wave-function. Instead of the wave-functions being described by the anti-symmetrized Slater determinant as they are in AMD, each nucleon is instead represented by a simpler Gaussian wave-function. The Gaussian wave-function, with width σ_r, is represented by [9]:

$$\mathrm{f_i}(\mathbf{r},\mathbf{p}) = \frac{1}{(2\pi\sigma_r\sigma_p)^3}\cdot\exp\left[-\frac{(\mathbf{r}-\langle\mathbf{r}\rangle_i)^2}{2\sigma_r^2}-\frac{2\sigma_r^2(\mathbf{p}-\langle\mathbf{p}\rangle_i)^2}{2\sigma_p^2}\right] \tag{2.4}$$

where r and p are the centers of the position and momentum of the nucleon and σ_r and σ_p are the dispersions in position and momentum space. The equations of motion for r and p are derived from the time-dependent variation principle. The EoS for CoMD are produced with a simple Skyrme interaction with compressibility of K=200 MeV and with the asymmetry energy included [8].

In CoMD, for every time-step and for each particle, an ensemble of the nearest particles is produced with distances of $3\sigma_r$ and $3\sigma_p$ in phase space. From this ensemble, the phase space occupation, $\overline{f}_i$, is determined. If $\overline{f}_i$ is greater than 1, the Pauli principle has been violated and as a result, the momenta of the particles in the ensemble is randomly changed while still conserving the total momentum and total kinetic energy. To reduce the number of calculations, instead of changing the momentum of the entire ensemble, only the particle of interest and the particle that contributes the largest to $\overline{f}_i$ are changed. This creates a two-body scattering, which is reasonably realized at small time-steps [9]. Addressing the Pauli principle in this manner introduces a repulsive force to the system. Once $\overline{f}_i$ is less than 1, the simulation proceeds to the next time-step. For each nucleon-nucleon collision, the final state phase space occupation is evaluated and accepted if less than 1, and rejected if greater than 1 [8]. The CoMD model has been further improved to include the conservation of angular momentum throughout the reaction [9].

The main differences between the AMD and CoMD models is the treatment of the wave-function and the Pauli principle. The Slater determinant wave-function used in AMD is more complicated than the Gaussian wave-function used in CoMD. Because of this, the AMD simulation has more calculations to perform and takes longer to produce events than CoMD. Because of the shorter computation time for each event, especially for larger systems, CoMD can run for a longer time and produce more statistics with the same amount of processing time. In this work, the CoMD was propagated to 3000 fm/c, allowing the system to cool dynamically. After 3000 fm/c, Gemini can be applied to cool any fragments that were not already de-excited.

2.4 Statistical Models

Statistical models describe the break-up of a thermally equilibrated nucleus from an excited state. These models de-excite the fragments from a nuclear reaction through fragmentation and particle emission. The de-excitation of the system depends on parameters such as the excitation energy, angular momentum, size, and N/Z of the system.

2.5 GEMINI

To study the effects of a statistical model, GEMINI was employed as an afterburner to de-excite the excited fragments produced from the dynamical models. The GEMINI model is a statistical decay model, which de-excites hot fragments based on their excitation energy, angular momentum, charge, and mass [12]. The fragments are de-excited by a series of sequential binary decays, considering all de-excitation possibilities from light charged particle emission to symmetric division. From this, a Monte Carlo method is used to follow the de-excitation of the fragment through the binary decays until the system can no longer decay. The decay widths for $Z \leq 2$ particles evaporated from the system are calculated using the Hauser-Feshbach formalism. For calculating the emission of heavier fragments from reactions involving particle emission, fragmentation, and binary decays, the Bohr-Wheeler formalism is used. In addition to fragment emission, gamma emission is also considered as a de-excitation channel, especially when the excitation energy is low and gamma and particle decay widths are similar. GEMINI++ is an updated version of the code that includes improvements in the calculation of the width of the charge and mass distributions from fission of heavy fragments. Although GEMINI++ has been used for all of the calculations, the original name, GEMINI, will be used to refer to the model in this work.

When using GEMINI, some assumptions are made about the input into the code. GEMINI assumes spherical sources at normal nuclear density (ρ_0=0.16 fm^{-3}) as its input. However, the results of the molecular dynamics simulations are often not spherical and are below normal nuclear density. The results of the source characteristics when inputted into GEMINI may affect the decay process calculated by GEMINI. Also, once GEMINI has produced the cooled fragments, they no longer interact by Coulomb or nuclear forces. While assumptions are made about the system when using GEMINI that do not reflect the true interactions of nucleons, the results from using GEMINI as an afterburner have shown to agree reasonably well with experimental observables [23,7].

2.6 Experiment

Fragments from the symmetric reactions of ^{64}Ni+^{64}Ni, ^{64}Zn+^{64}Zn, and ^{70}Zn+^{70}Zn at 35 MeV/nucleon were detected in the NIMROD-ISiS (Neutron-Ion Multidetector for Reaction Oriented Dynamics and Indiana Silicon Sphere) array [24,25] consisting of a 4π charged particle detectory housed inside the TAMU Neutron Ball at Texas A&M University Cyclotron Institute. The TAMU Neutron Ball is a neutron multiplicity detector comprised of four wedges and two hemispheres. An in depth study of the neutron ball efficiency has been performed using the GCalor code coupled to the GEANT-3 simulation package by Murray et al. [26]. The efficiency of the neutron ball was calibrated against a ^{252}Cf source.

The charged particle array consists of 14 concentric rings that cover an angular range of 3.6° to 167° in laboratory frame as shown in Figure 8. The charged particles are detected and identified by the use of silicon detectors in front of CsI(Tl) crystals to constitute a Si-CsI telescope. Two different types of telescopes were employed, a single silicon telescope, and a double silicon super-telescope. For both telescopes, the silicon detectors were mounted in front of a CsI crystal, which was attached to a photo-multiplier tube (PMT) for detectors in the forward hemisphere, or a photo-diode (PD) in the backward hemisphere. For the single silicon telescopes, silicon detectors of 150μm, 300μm, or 500μm were placed in front of a CsI crystal. For the super-telescopes, a 150μm Si was mounted in front of a 500μm silicon which was then followed by a CsI crystal. There are two super-telescopes in ring 2 of the charged particle array, and four super-telescopes in rings 3-9. The rest of the detectors are single silicon telescopes.

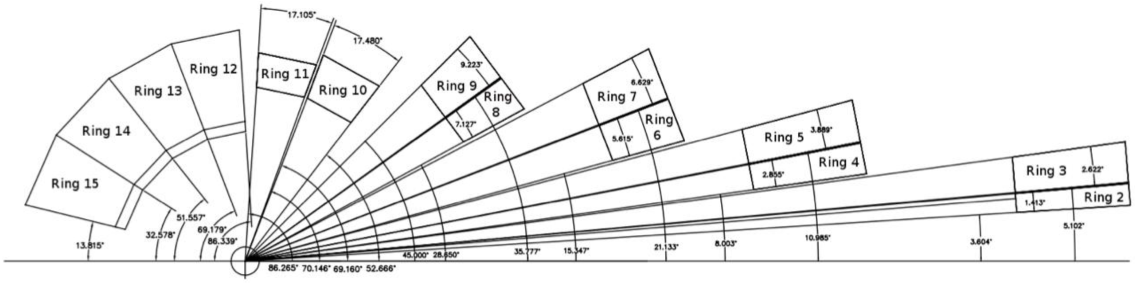

Figure 8. Side view of the NIMROD-ISiS charged particle array. Rings are labeled by their angular coverage in lab.

Charged particles were identified in the detector array by the use of the ΔE-E technique. For single telescopes, the energy lost in the silicon detector is ΔE, and the residual energy of the particle that stops in the CsI crystal is E. In the super-telescopes two ΔE-E quantities can be measured. The first ΔE-E signal was provided by the first silicon measuring the ΔE as the particle loses energy, and the second silicon detector measuring the residual E as the particle stopped in the 500μm silicon detector. A second ΔE-E signal was measured if the particle passed through the second silicon, so that the 500μm silicon measures the ΔE of the fragment and the CsI crystal measures the residual E. The inclusion of the super-telescopes in the charged particle array allows for measurement of isotopes of elements up to Z=17.

Plots of ΔE vs. E were created for each of the Si-Si and Si-CsI combinations in the charged particle array. Once these figures were created for each set of detectors, lines were hand-picked along each element in the plots to follow the curvature of the lines. Once the lines were created for each element, a spline fit was created along the user-defined line. The data was then linearized using these lines for each element to create a 2D plot of the linearization. This 2D linearization was then projected onto a 1D plot that results in distinct isotope peaks for each element. Gaussians are fit to each of these peaks to assess a yield and contamination with other isotopes. From these fits, each of the isotopes are defined and measured for each detector in the experimental data.

The experimental data was then calibrated to determine the correct energy of the fragments. The energy calibrations were done by comparing the results to a ^{228}Th source and to high-energy reactions of light projectiles. The use of the NIMROD-ISiS array allowed for a large amount of experimental data to be collected and provided good isotopic resolution of the data. After the energy calibrations, the experimental data could be used for analysis and comparison to the results from simulations.

2.7 Quasi-Projectile Reconstruction

Quasi-projectiles (QP) were reconstructed from the fragments produced in the simulations and fragments detected in the experiment. To reconstruct the QP, several cuts were made on the detected fragments to select a spherical source [19]. The first cut on the data is a velocity cut to remove fragments that are moving too fast or slow to be considered as coming from the QP. This selection is based on the velocity of each fragment relative to the longitudinal velocity of the largest fragment in an event, the projectile-like fragment (PLF) [27]. The fragments remain in the QP if the longitudinal velocity of the fragment is ±65% of the longitudinal velocity of the PLF for Z=1 fragments, ±60% for Z=2 fragments, and ±40% for Z≥3 fragments. The second cut on the data is to remove events based on the quadrupole moment of a momentum distribution in order to select only QP's that are nearly spherical in shape. The quadrupole moment is defined as the ratio of the sum of the longitudinal momenta squared to the the sum of the transverse momenta squared:

$$Q = \frac{\sum p_{z,i}^2}{\frac{1}{2}\sum p_{t,i}^2} \quad , \quad p_{t,i}^2 = p_{x,i}^2 + p_{y,i}^2 \tag{2.5}$$

The quadrupole moment, Q, is less than 1 for oblate QP, where the transverse momentum is larger than the longitudinal momentum, and is greater than 1 for prolate QP. When the log of Q is taken, the Q distribution is centered at 0, which represents spherical events where the transverse and longitudinal momenta are equal. The quadrupole cut selects nearly spherical QP’s that have a log(Q) value between -0.3 and 0.3. The final cut on the data is to select on the summed charge of the fragments. The sum of the charge in an event is selected to be near the charge of the projectile, so that the QP has a similar size as the projectile.

CHAPTER III
ANALYSIS

Multiplicity distributions, isotope distributions, charge and mass distributions, and isoscaling were studied from symmetric reactions of ^{64}Ni+^{64}Ni, ^{64}Zn+^{64}Zn, and ^{70}Zn+^{70}Zn at 35 MeV/nucleon. Fragments from the reactions were detected in the NIMROD-ISiS array. Simulations using AMD, CoMD, and GEMINI were also studied for the same reactions [24]. The fragment distributions and isoscaling analysis were studied in two ways. The first way that will be discussed is using inclusive distributions of all of the fragments from the event. The second way will be using only the fragments emitted from a reconstructed QP source. Each of these observables and analyses has been shown to have either a dependence on the asymmetry energy or a dependence on the time-step of a dynamical simulation.

3.1 Experimental Filter

To compare the simulations to the experimental data, an experimental filter was applied to the results from the simulations. The filter applied the same limits on the fragments from the simulations that are present in the experiment. A geometrical filter was used to simulate the geometry of the NIMROD-ISiS array, and energy cuts were used to limit the fragments to the energy range detected in the NIMROD-ISiS detectors. The filter also instituted a requirement of a multiplicity greater than 2 for each event and a total charge detected of at least 40% of the original system charge. Applying these cuts to the simulation allowed for a direct comparison of the filtered simulation results and the experimental results. The following analyses will use only filtered simulation results unless otherwise indicated.

3.2 Charge and Mass Distributions

Charge and mass distributions are shown for the results from each of the AMD, CoMD, and GEMINI simulations, as well as from experimental data. The AMD simulation is examined at time-steps of 300 fm/c, 3000 fm/c, and 300 fm/c with GEMINI used as an afterburner, while the CoMD simulation is examined at time-steps of 300 fm/c and 3000 fm/c. Figure 9 shows the charge distributions of fragments from the ^{64}Zn+^{64}Zn reaction from experimental data and AMD simulations. The relative yield is the multiplicity for each event, which is the yield of each element divided by the number of events in each of the simulations and experiment. A relative yield allows for the direct comparison of the simulations with the experimental data.

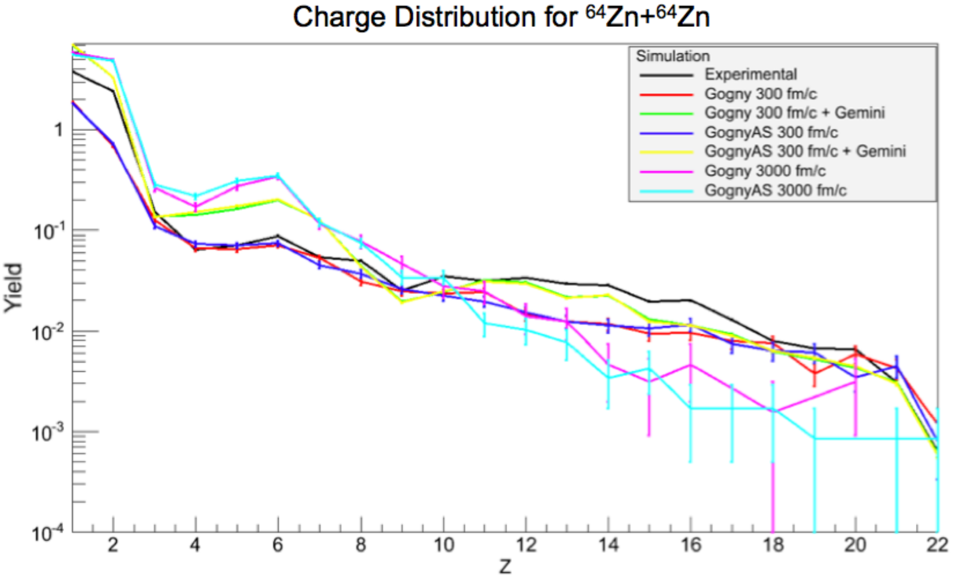

Figure 9. Charge distribution for ^{64}Zn+^{64}Zn reactions from experimental data and simulations of AMD Gogny and Gogny-AS at 300 fm/c, 3000 fm/c, and 300 fm/c with GEMINI.

In Figure 9, the peak of each distribution is at Z=1. The AMD at 300 fm/c has the lowest yield at Z=1 of about 2. The experimental data has a Z=1 yield of about 3. The AMD at 3000 fm/c and at 300 fm/c with GEMINI have a similar yield at Z=1 around 5. The majority of the distributions for each simulation and the experiment are in the range of light charged particles (LCP) from Z=1 to Z=2 and intermediate mass fragments (IMF) from Z=3 to Z~6. The AMD at 300 fm/c matches the experimental distribution the closest in the region of IMF. The AMD at 3000 fm/c and 300 fm/c with GEMINI have a higher yield of LCP and IMF than the experimental distribution. The charge distributions for the Gogny and Gogny-AS interactions at each time-step are very similar to each other, but the distributions are different for the different time-steps for each AMD simulation in the charge distribution. The charge distributions exhibit a dependence on the time-step of the simulation, but not on the asymmetry energy.

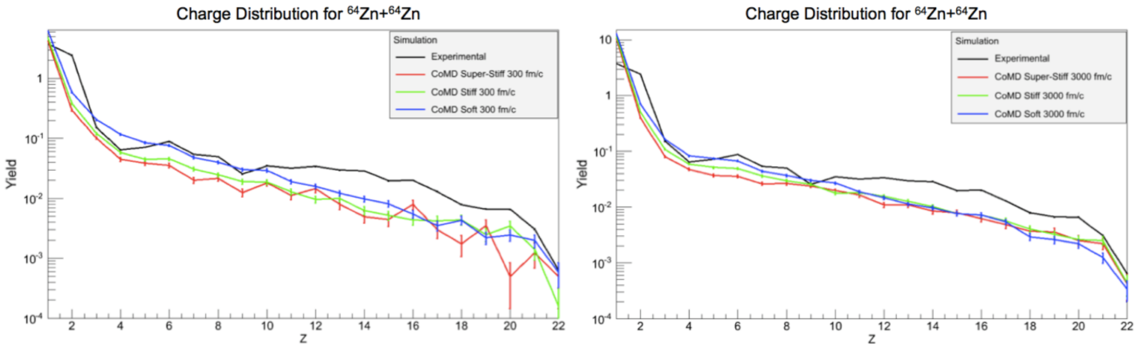

Figure 10. Charge distributions for ^{64}Zn+^{64}Zn reactions from experimental data and simulations of CoMD soft, stiff, and super-stiff at 300 fm/c and 3000 fm/c.

Figure 10 shows the charge distributions for the CoMD simulations at 300 fm/c and at 3000 fm/c. For the CoMD simulations and experimental data, the charge distributions peak at Z=1. The CoMD at 300 fm/c peaks between 4 and 6 while the CoMD at 3000 fm/c peaks around 10. At the later time-step of 3000 fm/c, there is a large increase in the amount of LCP from the simulation. The Z=1 yield of the CoMD at 300 fm/c is much closer to the yield of the experimental data than the CoMD at 3000 fm/c. The CoMD at both time-steps has a lower yield of Z=2 fragments compared to the experiment. For IMF and above, the charge distributions of the CoMD at 300 fm/c and 3000 fm/c match the experimental distribution similarly. The different interactions in CoMD have an ordering to their distributions, with the soft having a higher overall yield for LCP and IMF and the super-stiff having the lowest yield in this region. There is only a slight difference in the shapes of the charge distributions between the CoMD at 300 fm/c and 3000 fm/c, mostly evident in the yield of Z=1 fragments. The charge distributions for the CoMD simulations show an asymmetry energy dependence between the different interactions, but do not exhibit a large dependence on the time-step of the simulation.

Both the AMD and CoMD simulations show an increase in the production of LCP when comparing earlier time-steps (300 fm/c) to later time-steps (3000 fm/c). This corresponds to continuing fragmentation and particle emission in the reaction between 300 fm/c and 3000 fm/c as the system de-excites. While the AMD does not show a clear ordering of the interactions in the charge distributions at various time-steps, the interactions from the CoMD simulations show a clear ordering at both time-steps. The AMD simulations better approximate the yield of Z=2 fragments compared to the CoMD. This is shown in the slope between the Z=1 and Z=2 fragments, where the AMD has a shallow slope, similar to the experimental distribution, while the CoMD decreases sharply. Though none of the distributions from either model match the experimental distribution exactly, especially for Z=1 and Z=2, the 300 fm/c time-step in both AMD and CoMD seem to match the experimental distribution fairly well for fragments with $Z \geq 3$.

Mass distributions from the AMD and CoMD simulations of the ^{64}Zn+^{64}Zn reactions were compared to the experimental data. The mass distributions for the AMD simulations and the experimental data are shown in Figure 11 and follow the same general trends as the charge distributions. The yields for A=5 and A=8 fragments equal zero and the distribution is shown as continuous in these regions in order to connect the points on either side of these masses. The experimental distribution peaks for protons and neutrons at A=1 and peaks again at A=4 for alphas. The AMD simulations for each time-step match the shape of the experimental peaks at A=1 and A=4, though the relative yields are different. For LCP, the AMD at 300 fm/c with GEMINI agrees most closely to the experimental distribution, and for Z ≥ 3, AMD at 300 fm/c agrees most closely. As in the charge distributions, the Gogny and Gogny-AS interactions at each time-step do not show a large difference within error bars. There is a difference in the shape of

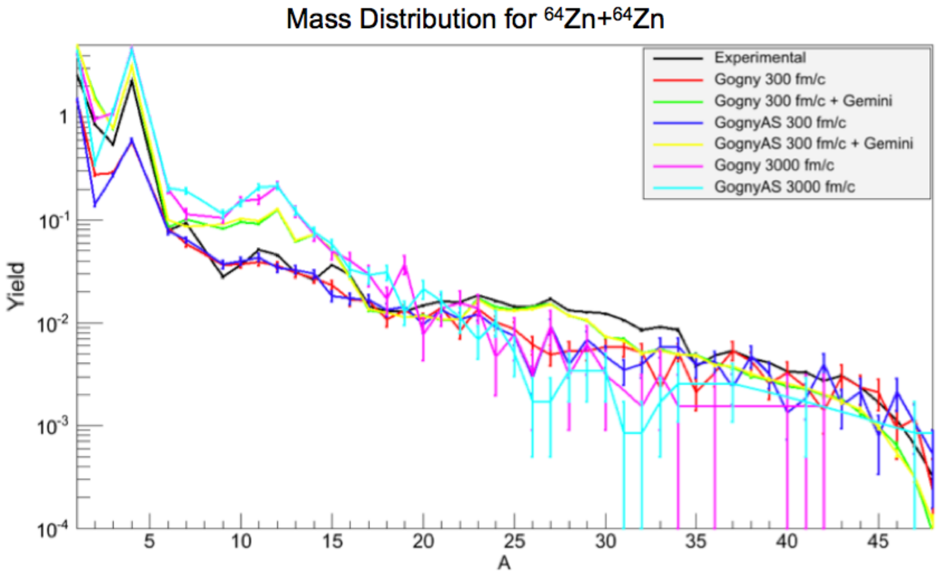

Figure 11. Mass distribution for ^{64}Zn+^{64}Zn reactions from experimental data and simulations of AMD Gogny and Gogny-AS at 300 fm/c, 3000 fm/c, and 300 fm/c with GEMINI.

the distributions between the AMD at 300 fm/c compared to the AMD at 3000 fm/c and at 300 fm/c with GEMINI, which have similar distributions. This exhibits a dependence on mass distribution with the time-step of the simulation in AMD.

Figure 12 shows the mass distributions for CoMD at 300 fm/c and 3000 fm/c with experimental data. The mass distributions peak at A=1 for protons and neutrons and show a general decrease in yield with increasing mass. The relative yield of protons and neutrons at A=1 in the CoMD at 300 fm/c is around 3 to 4, which is similar to the relative yield of the experimental data. The CoMD at 3000 fm/c has a much larger relative yield for protons and neutrons around 10. The mass distribution for CoMD at both time-steps agrees well with the experimental distribution except for alphas at A=4.

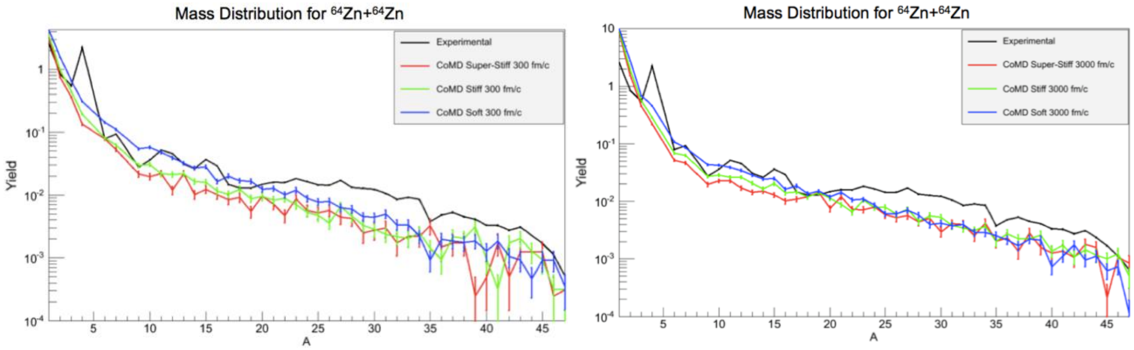

Figure 12. Mass distributions for ^{64}Zn+^{64}Zn reactions from experimental data and simulations of CoMD soft, stiff, and super-stiff at 300 fm/c and 3000 fm/c.

The main difference between the experiment and CoMD simulations is the yield of alpha particles, where the experimental distribution has a large peak at A=4 and the CoMD distribution decreases from A=3 to A=6 with little change in the slope. The soft, stiff, and super-stiff interactions follow an order, similar to the charge distribution, where the soft interaction has the highest yield of LCP and IMF and the super-stiff has the lowest yield.

As in the charge distributions, the mass distribution from the 300 fm/c time-step in AMD show good agreement with the experimental mass distribution, while the CoMD has a similar agreement with the experimental data for both time-steps. The CoMD has an ordering of the three interactions that follow the same ordering from the charge distributions, while the AMD does not show a difference between the Gogny and Gogny-AS interactions in the mass distributions. The main difference between the mass distributions of the two models is the treatment of protons, neutrons, and alphas in each model. The AMD simulations at each time-step follow the trend of the experimental distribution in regards to the increase in the yield of alphas relative to the yield of adjacent fragments. The CoMD does not show an increase in the production of alphas, but instead the distributions decrease continually in this region. The production of protons and neutrons differs between the two as well. In the CoMD, there is a noticeable jump in the production of A=1 fragments from 300 fm/c to 3000 fm/c, moving from a relative yield near the experimental yield to a yield of over three times the experimental yield. The AMD also shows an increase in A=1 fragments over time, but the change from 300 fm/c to 3000 fm/c or 300 fm/c with GEMINI is smaller and moves from a yield of about one A=1 fragment fewer per event to about two A=1 fragments more per event. The charge and mass distributions show a dependence on the time-step of the simulation in both AMD and CoMD, while only the CoMD shows a dependence on the asymmetry energy of the interactions.

3.3 Multiplicity Distributions

The multiplicity of a reaction is the number of fragments produced in the reaction. The total multiplicity of charged particles and neutrons from the experimental data and simulations of ^{64}Zn+^{64}Zn is shown in the multiplicity distributions. Figure 13 shows the multiplicity distributions of CoMD at 300 fm/c and 3000 fm/c with the experimental distribution.

In Figure 13, the experimental multiplicity data peaks around a multiplicity of 10. In the left part of Figure 13, the CoMD at 300 fm/c has a wide distribution, where the stiff and super-stiff interactions peak near a multiplicity of 10, and the soft interaction has two peaks, one at a low multiplicity and one at a high multiplicity. In the right part of Figure 13, the CoMD simulations at 3000 fm/c do not have a clear peak in the multiplicity distributions at all. There are very few events with a multiplicity below 8, and the distributions are generally flat and have a high multiplicity. The multiplicities

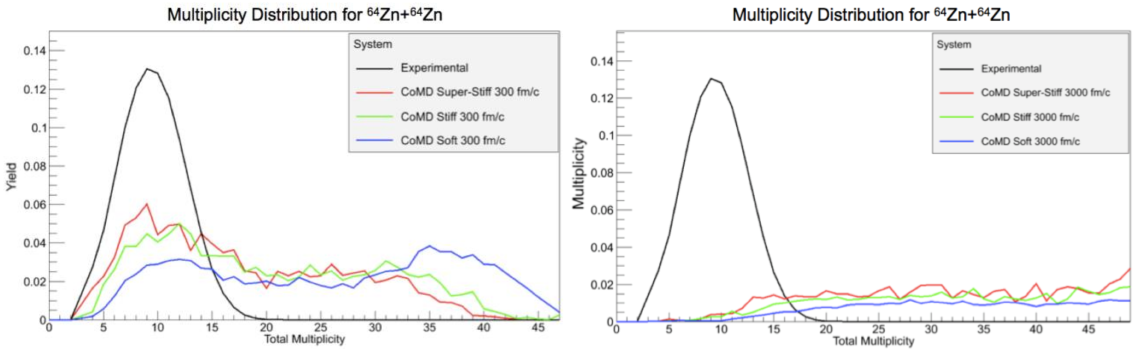

Figure 13. Multiplicity distributions for ^{64}Zn+^{64}Zn reactions from experimental data and CoMD soft, stiff, and super-stiff at 300 fm/c and 3000 fm/c.

from the CoMD simulations in Figure 13 are generally much higher than the experimental multiplicity. The higher multiplicity at the later time-step is consistent with fragmentation and particle emission from the reaction over time. The interactions from the CoMD simulations at both time-steps show an ordering in the multiplicity distributions. The super-stiff interaction has the highest relative yield in the 3000 fm/c, and a higher relative yield for lower multiplicity evens in the 300 fm/c. The soft interaction has the lowest relative yield in these regions, and the stiff interaction is generally in between the soft and super-stiff.

Figure 14 shows the multiplicity distribution of AMD with the experimental data. The multiplicity distribution of AMD at 300 fm/c peaks around a multiplicity of 12, similar to the multiplicity from the experiment. The multiplicity distributions for AMD at 3000 fm/c and 300 fm/c with GEMINI are peaked at a higher multiplicity near 40. The average and width of the multiplicity distribution for AMD at 300 fm/c match very well with the average and width of the experimental multiplicity distribution. The AMD at 3000 fm/c has a similar width as the experimental multiplicity distribution, but has a larger average multiplicity. The multiplicity distribution from AMD with GEMINI has a broader distribution than the purely dynamical simulations. Even though the AMD with GEMINI has a larger width than the AMD at 3000 fm/c, the average multiplicities are very close. This shows that the final multiplicities using a dynamical model to a long

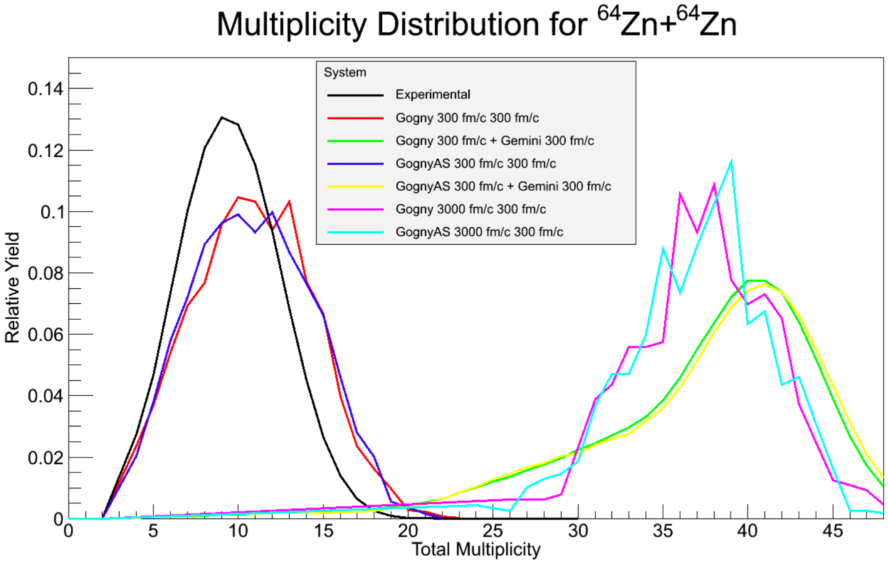

Figure 14. Multiplicity distributions for ^{64}Zn+^{64}Zn from experimental data and AMD Gogny and Gogny-AS at 300 fm/c, 3000 fm/c, and 300 fm/c with GEMINI.

time-step, or using a statistical model to de-excite the system from an earlier time-step, provide similar results. There is very little difference between multiplicity distributions of the Gogny and Gogny-AS interactions at each time-step.

Some of the difference in the widths of the AMD and CoMD multiplicity distributions can be attributed to the fragment emission preference of the two models. The charge and mass distributions show that CoMD has a high yield of protons and neutrons, especially at later time-steps, and AMD has a higher yield of alpha particles than the CoMD. Since CoMD produces more protons and neutrons relative to the AMD, and AMD produces more alpha particles relative to CoMD, the width of the multiplicity distributions for AMD is narrow. For a fixed mass, CoMD will produce more protons and neutrons from the system than the number of alpha particles AMD will produce, thus lowering the multiplicity of AMD for the same type of fragmentation.

3.4 Isotope Distributions

The isotope distributions show the yield of all of the isotopes of each element. Isotope distributions are shown for isotopes of elements Z=0 to Z=6 from ^{64}Zn+^{64}Zn reactions for AMD and CoMD simulations and the experimental data. The points are connected by lines to guide the eye. The isotopes for even numbered elements are shown in the top part of the figures, and isotopes for odd numbered elements are shown in the bottom part of the figures.

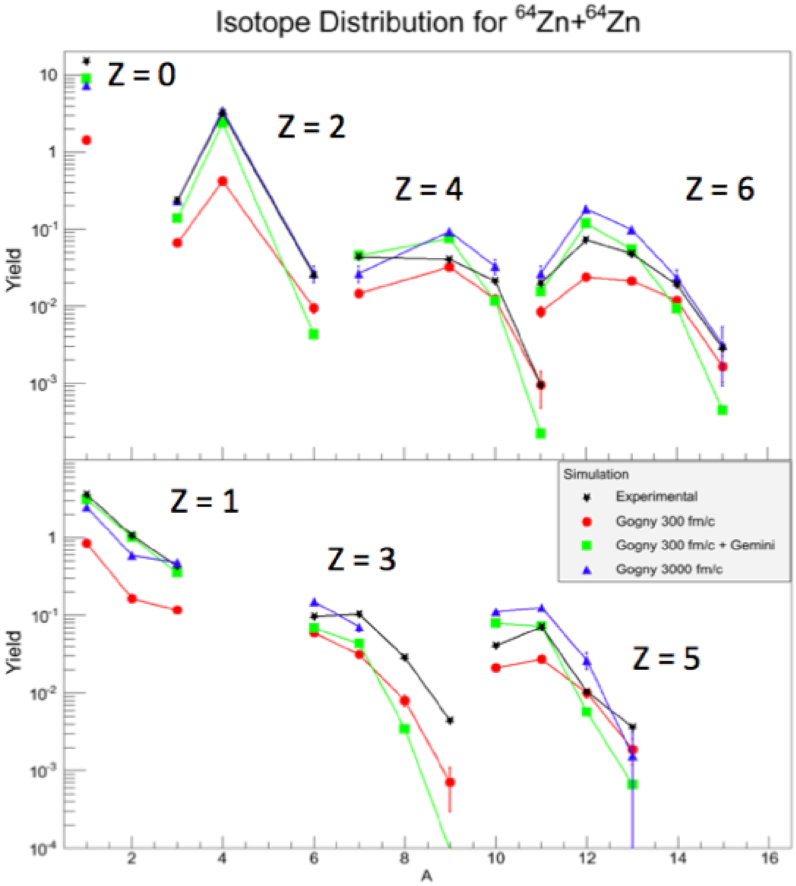

Figure 15. Isotope distributions for isotopes of elements Z=0 to Z=6 for ^{64}Zn+^{64}Zn reactions from experiment and AMD Gogny simulations at 300 fm/c, 3000 fm/c and 300 fm/c with GEMINI.

Figure 15 shows the isotope distributions for ^{64}Zn+^{64}Zn reactions from experiment and AMD Gogny interactions at 300 fm/c, 3000 fm/c, and at 300 fm/c with GEMINI. This shows how the isotope distributions for the Gogny interaction change with time and with the addition of a statistical model. For lighter isotopes, the isotope distributions from the Gogny interaction at 3000 fm/c and 300 fm/c with GEMINI match closer to the experiment than the AMD at 300 fm/c. For heavier isotopes, there is less of a difference between the different time-steps.

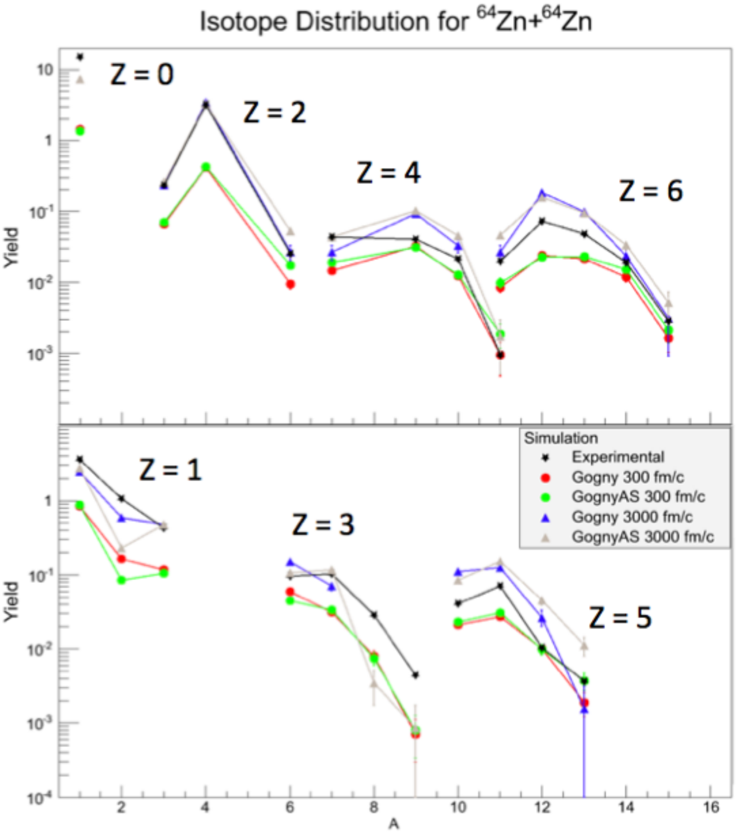

Figure 16. Isotope distributions for isotopes of elements Z=0 to Z=6 for ^{64}Zn+^{64}Zn reactions from experiment and AMD Gogny and Gogny-AS simulations at 300 fm/c and 3000 fm/c.

Figure 16 shows the asymmetry energy dependence of the isotope distributions for Gogny and Gogny-AS interactions at 300 fm/c and 3000 fm/c. The AMD at 3000 fm/c generally matches the experimental isotope distribution better than the AMD at 300 fm/c for both interactions, especially for light isotopes, also shown in Figure 15. There is not a large dependence on the asymmetry energy in the isotope distributions at either time-step. For various elements, the Gogny and Gogny-AS each match the isotope distributions, so no overall conclusion can be made about the agreement of the experiment and a specific interaction.

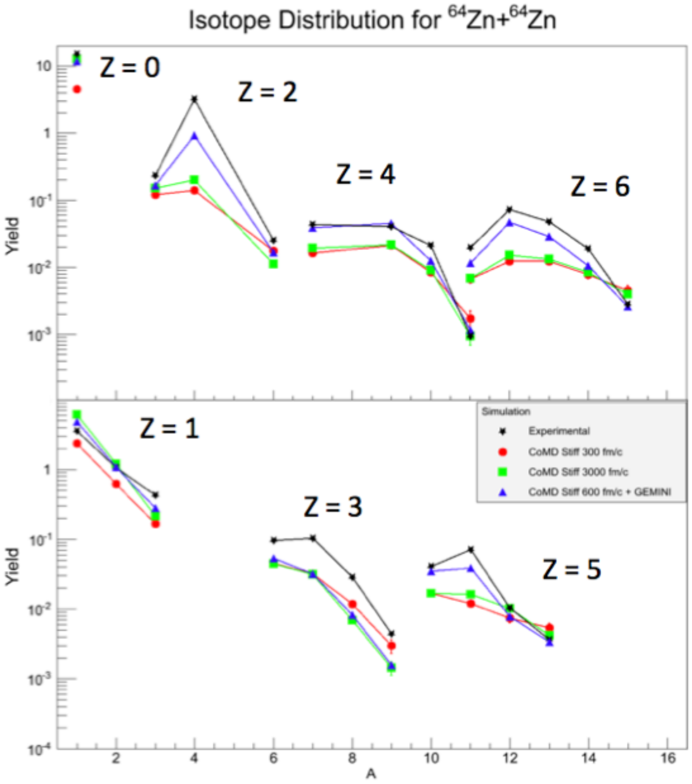

Figure 17. Isotope distributions for isotopes of elements Z=0 to Z=6 for ^{64}Zn+^{64}Zn reactions from experiment and CoMD stiff simulations at 300 fm/c, 3000 fm/c, and 600 fm/c with GEMINI.

Figure 17 shows isotope distributions for ^{64}Zn+^{64}Zn reactions from experiment and CoMD stiff simulations at 300 fm/c, 3000 fm/c, and 600 fm/c with GEMINI. This shows the dependence on the time-step of the simulation and the addition of GEMINI for the CoMD stiff interaction. The GEMINI code is applied to the CoMD simulation at 600 fm/c instead of 300 fm/c due to large angular momentum at 300 fm/c that is reduced by 600 fm/c. In general, the CoMD at 600 fm/c with GEMINI has higher yields than the CoMD at 300 fm/c and at 3000 fm/c. These higher yields match the yields of the experiment much better, especially for lighter isotopes and for even numbered elements. There is not a large difference between the isotope distributions for the stiff interaction at 300 fm/c and 3000 fm/c, but the inclusion of GEMINI causes a large upward shift in the distributions, especially for the most dominant isotope.

Figure 18 shows the asymmetry energy dependence of the isotope distributions from the CoMD simulations at 3000 fm/c. The soft, stiff, and super-stiff interactions are shown with the experiment. There is a clear ordering and separation of the interactions in the CoMD simulations at 3000 fm/c. The CoMD soft interaction has a higher yield than the stiff and super-stiff interactions across all of the elements with $Z \leq 6$. Because of this, the soft interaction matches the experimental isotope distributions better than the stiff and super-stiff interactions. This agreement is present mostly in the lighter isotopes and the most prominent isotope of each element.

The isotope distributions are shown with respect to the time-step dependence and the asymmetry energy dependence for the AMD and CoMD simulations relative to the experiment. There is relatively no asymmetry energy dependence shown in the AMD simulations, and a small asymmetry energy dependence shown in the CoMD results, with the soft interaction matching the experiment the closest. The time-step of the simulation, and specifically the addition of the GEMINI statistical decay model, has a large effect on the isotope distribution. In the AMD simulation, the AMD at 3000 fm/c and at 300 fm/c with GEMINI agree better with the experiment than the AMD at 300 fm/c, especially for light isotopes. For the CoMD simulation, the addition of GEMINI changes the yield of the isotopes greatly and matches the experimental distributions

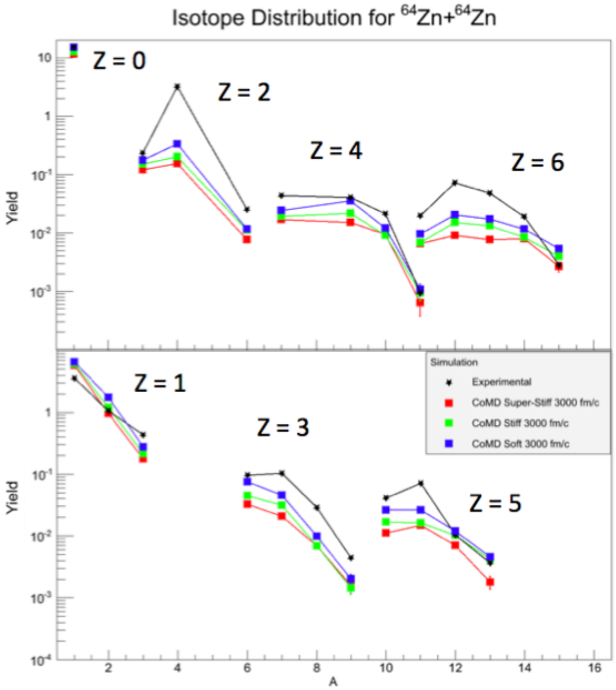

Figure 18. Isotope distributions for isotopes of elements Z=0 to Z=6 for ^{64}Zn+^{64}Zn reactions from experiment and CoMD soft, stiff, and super-stiff simulations at 3000 fm/c.

much closer. In general the asymmetry energy dependence varies for the AMD and CoMD simulations, but the AMD and CoMD with GEMINI show a much better agreement with the experiment.

3.5 Isoscaling

Isoscaling has also been studied using simulations and experimental data. For each of simulations and the experimental data, isotope yields were studied for each isotope in the reaction. The ratio of the yields was then determined by dividing the isotope yield from a neutron-rich system by the isotope yield of a neutron poor system. For systems of ^{64}Ni+^{64}Ni (N/Z=1.29), ^{64}Zn+^{64}Zn (N/Z=1.13), and ^{70}Zn+^{70}Zn (N/Z=1.33), the three isoscaling relations are ^{70}Zn+^{70}Zn/^{64}Zn+^{64}Zn,

^{70}Zn+^{70}Zn/^{64}Ni+^{64}Ni, and ^{64}Ni+^{64}Ni/^{64}Zn+^{64}Zn. Ratios of the isotope yields are produced to follow the isoscaling ratio, such that:

$$R_{21}(N,Z) = \frac{\text{Yield}_2(N,Z)}{\text{Yield}_1(N,Z)} \tag{3.1}$$

where Yield$_2$(N,Z) are the isotope yields for the neutron-rich system, Yield$_1$(N,Z) are isotope yields for the neutron-poor system, and R_{21}(N,Z) is the isoscaling ratio. For each isotope, the log of the isoscaling ratio for each isotope in the system is plotted against the number of neutrons in the isotope.

Figure 19 shows isoscaling of ^{70}Zn+^{70}Zn on ^{64}Zn+^{64}Zn from the AMD Gogny-AS simulation at 300 fm/c. The log of the isoscaling ratio for each isotope for each element is shown as a point with respect to the number of neutrons in the isotope. The

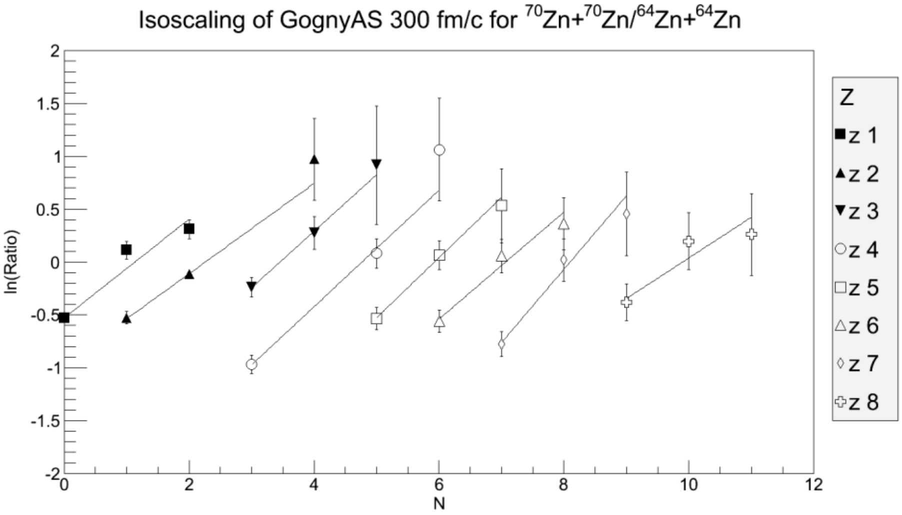

Figure 19. Isoscaling of ^{70}Zn+^{70}Zn/^{64}Zn+^{64}Zn for AMD Gogny-AS at 300 fm/c.
for each element. The slope of this line is α from Eq. 1.5.

fragment yields used in the isoscaling ratio are required to have a minimum of 15 events to reduce the error bars and select on fragments with a reasonable yield. Plotting the isoscaling yield on a log scale allows for a line to be fit through the isotopes.

In Figure 19, each element has a slightly different α value, but overall the α values are relatively close to each other and the lines are nearly parallel. If the isotopes are plotted against the proton number instead of the neutron number, the fits of the elements would be negative and the slope would equal β from the Eq. 1.5. When the isoscaling ratio is plotted against the number of neutrons, the magnitude of β is the spacing between the fits of the elements.

A global fit can be produced that takes into account both α and β by fitting to Eq. 1.5. The global fit is a two-dimensional fit instead of a one-dimensional fit as in Figure 19, and plots the neutron number and proton number on the x and y axes, and the natural log of the ratio on the z-axis. An exponential is then fit to these three values. From this fit, a global α and β can be extracted that fits all of the isotopes of all of the elements at the same time. Figure 20 shows the isoscaling of ^{70}Zn+^{70}Zn/^{64}Zn+^{64}Zn for AMD Gogny-AS simulation at 300 fm/c as before, but fit with the global α value instead of individual fits.

In Figure 20, the slopes for each element are replaced with slope of the global isoscaling α value that is obtained from the global fit. The global fit allows for the ability to extract one α value from the plot, which can represent the isoscaling of all of the fragments from ^{70}Zn+^{70}Zn on ^{64}Zn+^{64}Zn for the AMD Gogny-AS simulation at 300 fm/c. To better visualize how well this α value represents the individual values for each element, the global α value can be plotted relative to the slopes of each of the elements.

In Figure 21, the individual α values from the individual fits to the slopes from Figure 19 are plotted as filled circles. The global isoscaling value α extracted from the global fit for ^{70}Zn+^{70}Zn over ^{64}Zn+^{64}Zn with AMD Gogny-AS at 300 fm/c is plotted as a line. The global α value fits reasonably well to the individual α values, especially at low Z. Figure 22 shows the same relation, but now with all of the isoscaling systems.

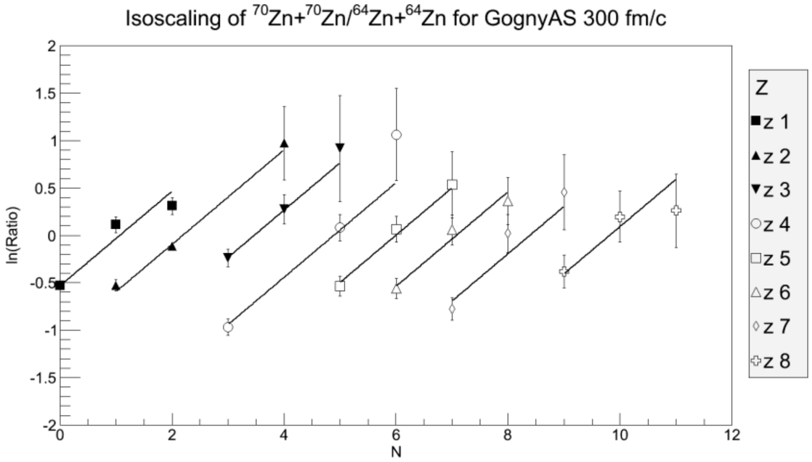

Figure 20. Isoscaling of ^{70}Zn+^{70}Zn/^{64}Zn+^{64}Zn for the AMD Gogny-AS simulation at 300 fm/c with the global α value, 0.5, used for the fit.

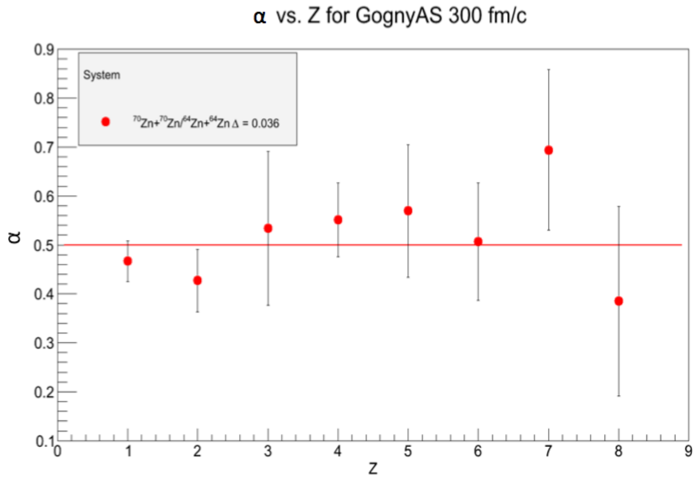

Figure 21. Isoscaling parameter α vs. element number, Z, for ^{70}Zn+^{70}Zn/^{64}Zn+^{64}Zn for AMD Gogny-AS at 300 fm/c, where circles are the individual α values from isoscaling in Fig. 11, and the line is the global α value, 0.5.

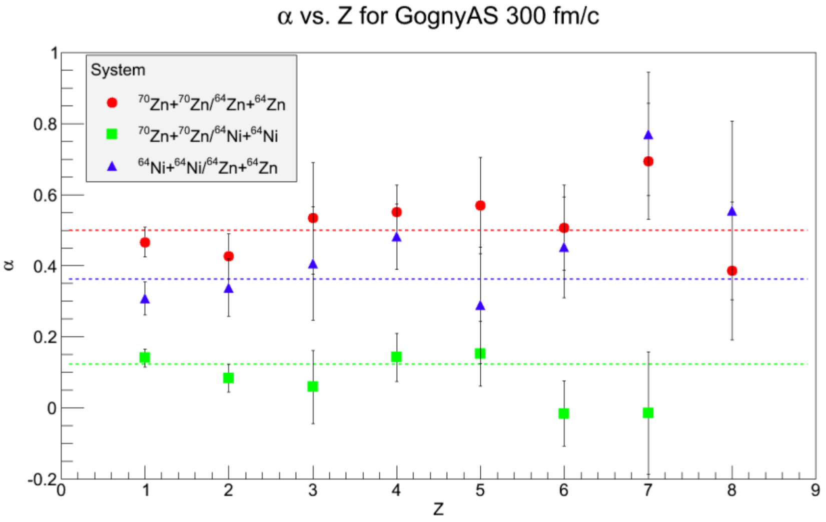

Figure 22. Isoscaling parameter α vs. element number, Z, for all three isoscaling systems for AMD Gogny-AS at 300 fm/c, where the points are the individual α values from isoscaling and the lines are the global α values.

The α value for each element is plotted as a solid point for each isoscaling system, and the global α value for each system is plotted in the same color as the individual α values. The magnitude of the global α value is shown to depend on the systems used in the isoscaling. The dependence of α on the isoscaling systems is shown in Eq. 3.2, where the isoscaling parameter, α, depends on the neutron-to-proton ratio of the systems:

$$\alpha = \frac{4C_{sym}}{T}\Delta \quad , \quad \Delta = \left(\frac{Z_1}{A_1}\right)^2 - \left(\frac{Z_2}{A_2}\right)^2 \tag{3.2}$$

In this equation, the α value obtained from the slopes of the fits to elements in isoscaling is related to C_{sym}, the symmetry energy coefficient from the binding energy equation, the temperature, T, and the charge to mass ratio, Δ, between the two sources used in the isoscaling ratio, where the first charge-to-mass ratio represents the neutron-poor system, and the second ratio represents the neutron-rich system.

The introduction of Δ allows for the comparison of isoscaling of multiple systems at the same time. The Δ for the isoscaling ratio was calculated by squaring the average (Z/A) of the system. The average (Z/A) of the system is found by taking the mean of the (Z/A) distribution, which is created by taking the ratio of the total charge of detected fragments in an event to the total mass, including neutrons, for detected fragments in an event. This mean value is the (Z/A) of the reaction and is squared to calculate the Δ value for each isoscaling system. As the Δ value decreases and the neutron-to-proton ratio of the systems used in isoscaling become closer together, the isoscaling parameter α also decreases. Figure 23 shows AMD and CoMD simulations for reactions of ^{70}Zn+^{70}Zn/^{64}Zn+^{64}Zn.

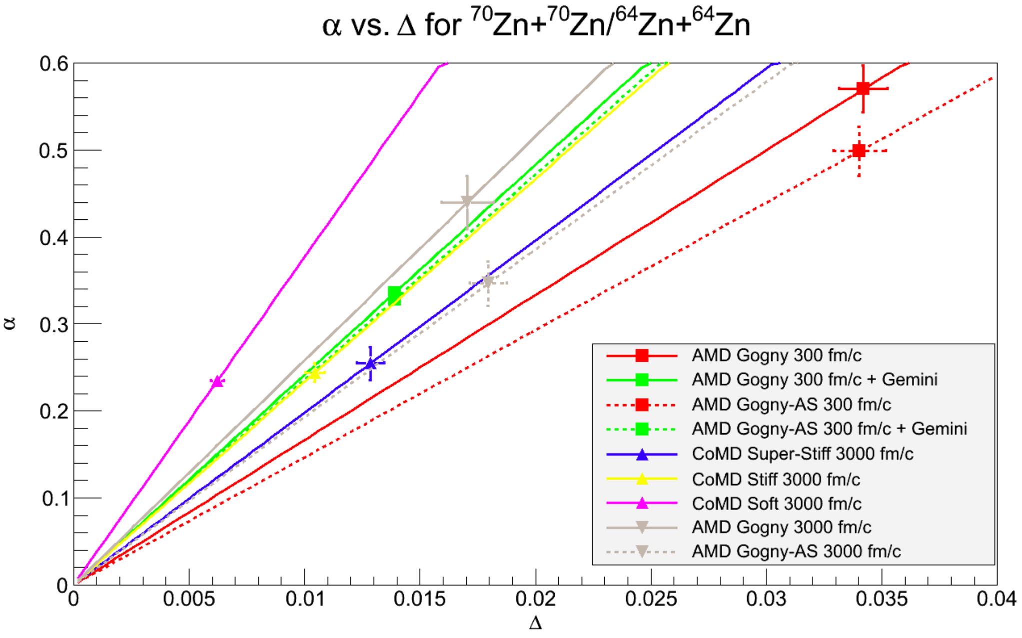

Figure 23. α vs. Δ from isoscaling of ^{70}Zn+^{70}Zn/^{64}Zn+^{64}Zn. For AMD, solid lines are Gogny and dashed lines are Gogny-AS.

The global α from isoscaling is plotted against Δ, and the lines are a fit to each point for each simulation and forced to go through the origin, since for a Δ of zero, α equals zero. Figure 23 shows the resulting α vs Δ plot for the isoscaling of the

^{70}Zn+^{70}Zn/^{64}Zn+^{64}Zn system for each of the simulations and the experiment . For a constantC$_{sym}$ and T the α and Δ have a linear relationship, which provides a way to observe multiple systems on the same plot. The linear relationship of α and Δ can be seen in Figure 24 as well, where multiple systems are combined into a single plot.

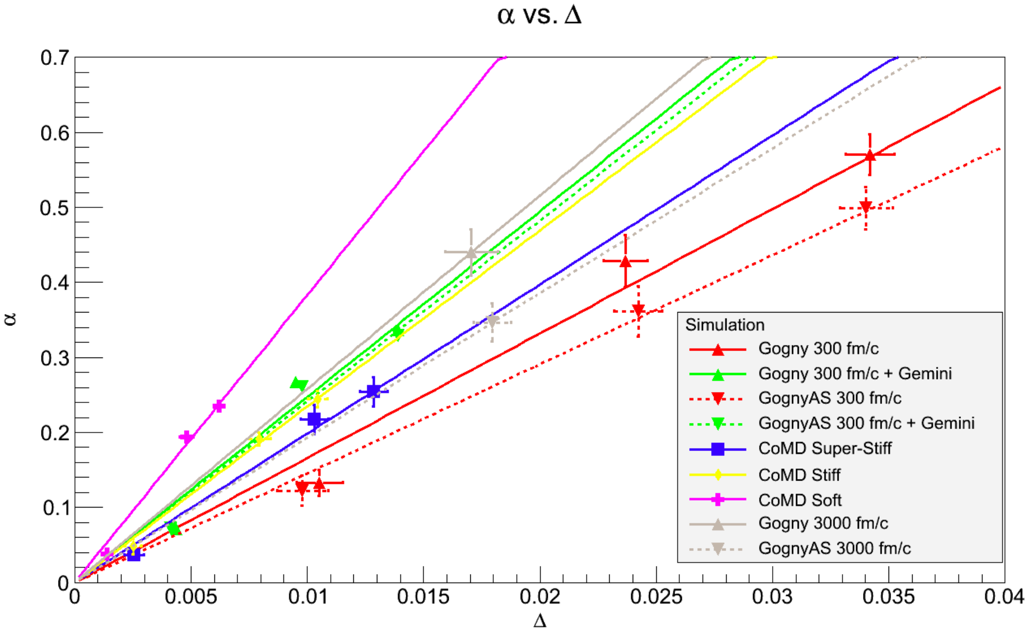

Figure 24. α vs. Δ from isoscaling of ^{70}Zn+^{70}Zn/^{64}Zn+^{64}Zn, ^{70}Zn+^{70}Zn/^{64}Ni+^{64}Ni, and ^{64}Ni+^{64}Ni/^{64}Zn+^{64}Zn. For AMD, solid lines are Gogny and dashed lines are Gogny-AS.

Figure 24, shows the α vs Δ from the isoscaling systems of ^{64}Zn+^{64}Zn/^{64}Ni+^{64}Ni, ^{70}Zn+^{70}Zn/^{64}Zn+^{64}Zn, and ^{70}Zn+^{70}Zn/^{64}Ni+^{64}Ni. The simulations are represented by the same line styles and colors as Figure 23. The points are the isoscaling results from all three systems, and lines now represent the fits to the results from all of the isoscaling combinations with the lines forced through the origin. For AMD at 3000 fm/c, only the ^{70}Zn+^{70}Zn/^{64}Zn+^{64}Zn isoscaling system was studied. With all three isoscaling systems included, the linear relationship between α and Δ can be seen. For example, the points of the CoMD soft interaction, shown as purple crosses, provide three points for the α vs. Δ values of three isoscaling systems, but all three points lie on a line that can be drawn through the origin. This linear relationship provides the ability to compare multiple isoscaling systems and multiple simulations at once.

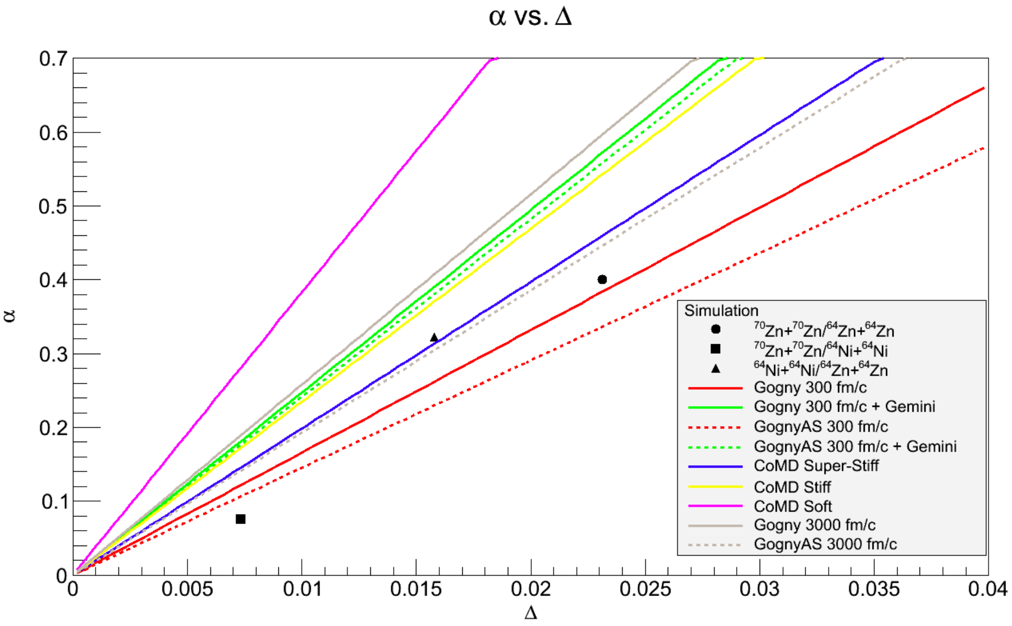

Figure 25. α vs. Δ with experimental data from isoscaling of ^{70}Zn+^{70}Zn/^{64}Zn+^{64}Zn, ^{70}Zn+^{70}Zn/^{64}Ni+^{64}Ni, and ^{64}Ni+^{64}Ni/^{64}Zn+^{64}Zn. For AMD, solid lines are Gogny and dashed lines are Gogny-AS.

Figure 25 shows the same data as in Figure 24, but with the individual data points removed and the experimental points included. The combined α vs Δ plot is very similar to the α vs Δ for the single system in Figure 23, suggesting that there is a good linear relationship between α and Δ with these systems. In Figure 25, the lines calculated from AMD at 300 fm/c are lower than those from AMD at 3000 fm/c, 300 fm/c with GEMINI, and CoMD at 3000 fm/c. This shows a difference in the isoscaling observed for dynamical models at short time-steps compared to longer time-steps and with using GEMINI as an afterburner. In the AMD simulations, there is a clear distinction between the Gogny and Gogny-AS interactions, with the softer Gogny interaction providing a larger slope than the stiffer Gogny-AS interaction for all time-steps. In the CoMD simulations, the super-stiff interaction has the largest slope, with the stiff and soft interactions having progressively smaller values. The experimental data lie close to the results from several simulations and do not exclusively agree with one simulation or time-step.

The effect of the time-steps of the simulations on the results from isoscaling is shown in the results from the AMD simulations. The AMD at 300 fm/c produces an isoscaling α value that is on average lower than the experimental data, while the AMD at 300 fm/c with GEMINI and AMD at 3000 fm/c produce an isoscaling α value higher than the data. This shows a clear dependence of the isoscaling on the time-step of the simulation, shown in the AMD from 300 fm/c to 3000 fm/c. Even though a comparison to the experiment may not be made, the trend of a decrease in the isoscaling parameter, α, with the time-step of the simulation is very clearly shown.

To further explore the dependence of the isoscaling parameter, α, on the time-step of the simulation, separate from the Δ value, a comparison of the isoscaling parameter α with respect to time is shown in Figure 26 for the ^{70}Zn+^{70}Zn/^{64}Zn+^{64}Zn isoscaling system. The same simulations are shown in Figure 26 as in the α vs Δ plot in Figure 25, except for the AMD Gogny at 3000 fm/c due to low statistics. The data for AMD 300 fm/c with GEMINI and the experimental data are shown at 3000 fm/c. As in Figure 16, the AMD at 300 fm/c has a larger α value than the experimental data, while the rest of the simulations have a lower α value. The α value for the AMD changes significantly over time for the Gogny-AS interaction, moving from around 0.5 to 0.35. The CoMD simulations show a less dramatic difference in the α value over time, staying near the same value from 300 fm/c through 3000 fm/c. The α value for AMD at 300 fm/c with GEMINI is very near to the α value for AMD at 3000 fm/c. This suggests that the de-excitation of the system in the AMD model, either by a dynamical process shown

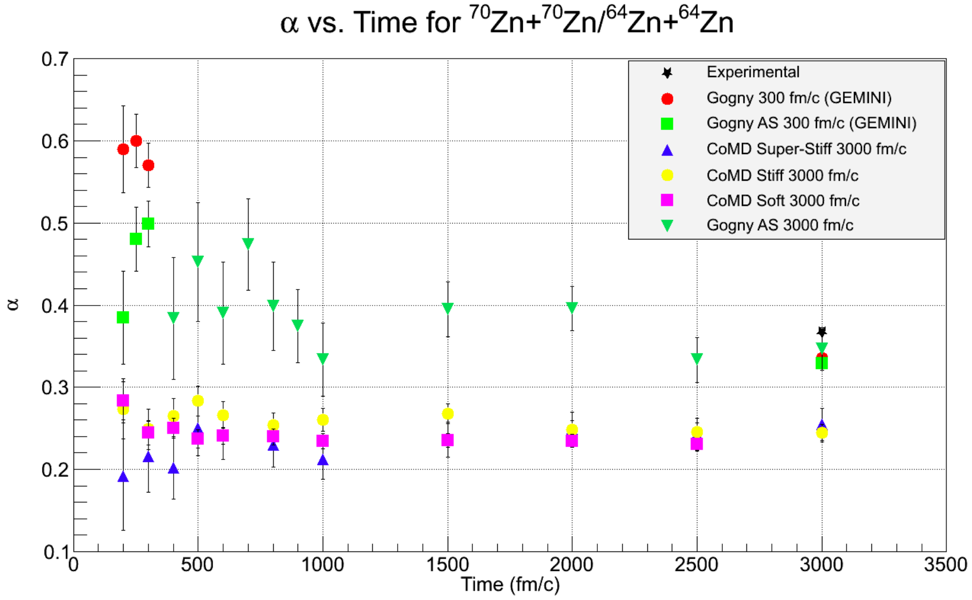

Figure 26. Isoscaling parameter α vs. time for ^{70}Zn+^{70}Zn/^{64}Zn+^{64}Zn. AMD 300 fm/c with GEMINI and experimental data are plotted at 3000 fm/c along with the final outputs of the AMD and CoMD at 3000 fm/c.

by the AMD at 3000 fm/c, or by a statistical de-excitation, shown by the AMD at 300 fm/c with GEMINI, does not affect the result of the isoscaling parameter, α. While the dependence on the type of de-excitation does not seem to matter in isoscaling, there is a clear dependence on the difference between the AMD simulation at an early time-step and a later time-step. The α values from the AMD simulation are in general higher than the α values from the CoMD simulation. In this plot, the isoscaling from the AMD simulations at 3000 fm/c and at 300 fm/c with GEMINI show the closest agreement to the isoscaling of the experimental data.

3.6 Quasi-Projectile

Instead of analyzing the fragmentation of the entire system, the fragmentation of a single source from the reaction can be studied. A quasi-projectile (QP) source is created in non-central collisions of the projectile and target, where the projectile interacts with the target and exchanges nucleons. After the interaction, the QP is similar in composition to the projectile, but may be larger or smaller due to the exchange of nucleons with the target. The QP is also excited at this point due to the collision and exchange of nucleons. The QP de-excites by fragmentation and particle emission. When these fragments are detected, they can be used to reconstruct the excited QP just before break-up to produce an equilibrated, spherical source. Analyzing the fragmentation of a single source has been shown to improve the isoscaling analysis [19] and allows for the observation of fragments coming from a single source instead of from multiple parts of the reaction. Reconstruction of the QP uses three cuts that define what fragments and events are included in the QP: the velocity cut, the quadrupole cut, and the sum charge cut.

The first cut is the velocity cut, which excludes particles from the QP reconstruction that are moving too fast or slow to belong to the QP. This cut is implemented by removing fragments based on their longitudinal velocity, or parallel velocity, relative to the longitudinal velocity of the heaviest fragment in the event. Three charge ranges were established and relative velocities were chosen based on those charges, such that if the longitudinal velocity of the fragment is ±65% of the longitudinal velocity of the heaviest fragment for Z=1, ±60% for Z=2, and ±40% for Z≥3, the fragments are included in the event. Any other fragments have too small or large of a velocity to be considered as emitted from the QP and are not included in the reconstruction.

The next cut, the quadrupole cut, selects QP's that are roughly spherical in shape. This is accomplished by using the collective momenta of the fragments from the reaction. The longitudinal momenta of the fragments, p_z, is compared to the transverse momenta, p_t, by the equation:

$$Q = \frac{p_z^2}{\frac{1}{2}p_t^2} \quad , \quad p_t^2 = p_x^2 + p_y^2 \tag{3.3}$$

such that Q=1 for perfectly spherical events. Events are then selected using a distribution of the log of Q, where the spherical events are now at log Q=0 and limits of -

0.3 to 0.3 are set on either side of the peak of the distribution to remove non-spherical events. Events with a negative Q have a larger transverse momentum than longitudinal momentum, and events with a positive Q have a larger longitudinal momentum than transverse momentum. Once the Q cut is applied, the remaining events are spherical in nature.

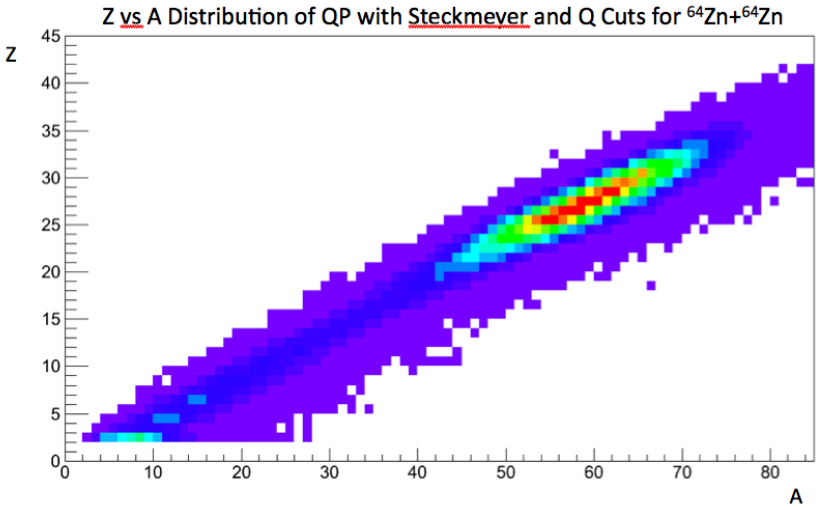

Figure 27. Charge vs. mass distribution for QP's with the velocity and quadrupole cuts applied from experimental data of ^{64}Zn+^{64}Zn.

The last cut is the sum charge cut, which selects QP’s that have a charge similar to that of the projectile. This cut is made after the velocity and quadrupole cuts are implemented and selects a range in Z of already spherical QP’s.

A charge vs. mass plot can be made that shows the QP's that still exist after the velocity and quadrupole cuts are made. These QP's are shown in Figure 27, where the mass is plotted on the x-axis and the charge is plotted on the y-axis. The charge cut selects events that have a similar charge as the projectile so that the QP has similar properties as the projectile. The charge cut was selected to provide a large amount of statistics, yet still only use the peak of the distribution of sources. For this work, a range in Z from 21 to 33 was used to collect the peak of the distribution of QP's near the charge of the projectile. With this defined QP, fragment distributions of fragments emitted from the QP and isoscaling of the QP can be studied.

3.7 QP Charge and Mass Distributions

Charge and mass distributions were created for the fragments emitted from the QP. Because the QP is defined as equilibrated and spherical, the fragments can be thought of as emitted isotropically from the source. Charge distributions were created with the same models and time-steps as previously described in the inclusive data. The yield is determined by dividing the yield, or multiplicity, of a given charge or mass by the number of QPs for each of the simulations and experimental data.

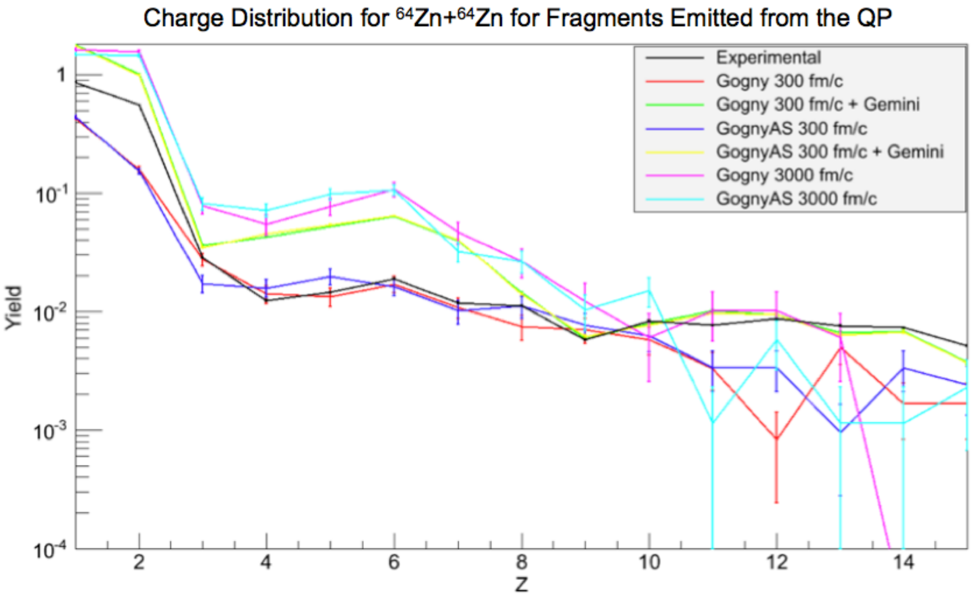

Figure 28. Charge distribution for fragments emitted from the QP for ^{64}Zn+^{64}Zn reactions from experimental data and AMD simulations at 300 fm/c, 3000 fm/c, and 300 fm/c with GEMINI.

The charge distributions for ^{64}Zn+^{64}Zn reactions from the experiment and AMD simulations are shown in Figure 28. The experimental distribution peaks at Z=1, has a slight decrease to Z=2, and has a much lower yield for Z=3 and greater. Each of the AMD simulations follow this trend for Z=1 and Z=2 with a much lower yield after Z=2. All of the AMD simulations match similarly well to the LCP region of the experimental distribution, but the AMD at 300 fm/c matches over a greater range of the entire charge distribution. The AMD at 300 fm/c has a lower yield of LCP and IMF than the AMD at 3000 fm/c and 300 fm/c with GEMINI, which are fairly close to each other. The charge distribution for fragments from the QP does not show a difference in the Gogny and Gogny-AS interactions within error bars for the AMD simulation.

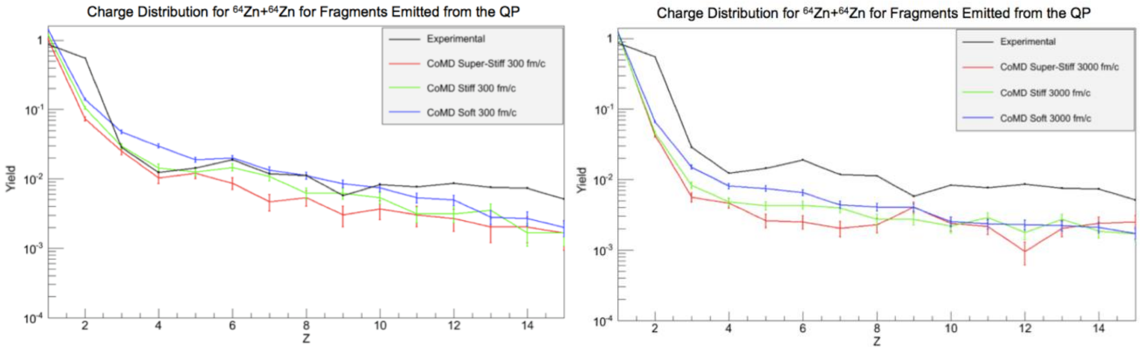

Figure 29. Charge distribution for fragments emitted from the QP for ^{64}Zn+^{64}Zn reactions from experimental data and CoMD simulations at 300 fm/c and 3000 fm/c.

Charge distributions for ^{64}Zn+^{64}Zn reactions from the CoMD simulations for 300 fm/c and 3000 fm/c and the experimental data are shown in Figure 29. The CoMD distributions at both time-steps peak at Z=1 and decrease in yield with higher mass. The CoMD at 300 fm/c agrees with the experimental distribution very well except at Z=2. The CoMD at 3000 fm/c has a lower yield than the experimental data over the entire Z range, except at Z=1. The soft, stiff, and super-stiff interactions show an ordering at both time-steps, where the soft interaction has a higher yield compared to the stiff and super-stiff interactions. In the charge distributions for CoMD at 300 fm/c, the different interactions have a very similar yield to the experimental data, but there is not a specific interaction that agrees with the experiment better than the other.

The charge distributions show a similar trend in the reconstructed QP data as with the inclusive data. The AMD does not show a difference in the Gogny and Gogny-AS interactions, while the CoMD shows a clear ordering of the soft, stiff, and super-stiff interactions. There does not seem to be agreement between the experimental data and any particular interaction from the AMD and CoMD simulations. The dependence on the time-step of the simulation is also very evident in the charge distributions from the reconstructed QP, as it was in the non-reconstructed data. For each of the models, yields of LCP and IMF at 300 fm/c were overall lower than at 3000 fm/c and in general agreed better with the experimental data.

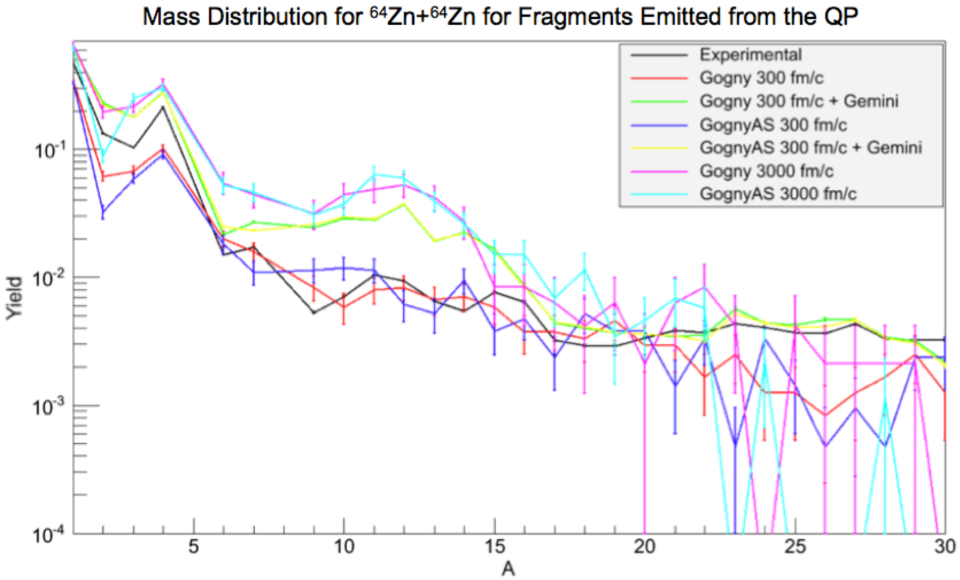

Figure 30. Mass distribution for fragments emitted from the QP for ^{64}Zn+^{64}Zn reactions from experiment and AMD simulations at 300 fm/c, 3000 fm/c, and 300 fm/c with GEMINI.

Mass distributions for the fragments emitted from the QP have also been created with the same models and time-steps as the charge distributions. Figure 30 shows the mass distributions for the AMD simulations and experimental data. The A=5 and A=8 masses are excluded and lines are drawn through these points to connect the adjacent masses. The experimental distribution and AMD simulations show a peak at A=1 for protons and neutrons and at A=4 for alpha particles. Through A=6, all of the mass distributions of the AMD simulations match the experimental mass distribution equally well. The AMD at 300 fm/c has a lower yield than the AMD at 300 fm/c with GEMINI and 3000 fm/c. After A=6, the AMD at 300 fm/c matches the experimental distribution very well in comparison to the AMD at 300 fm/c with GEMINI and 3000 fm/c. The Gogny and Gogny-AS interactions do not show a noticeable difference for any of the AMD simulation time-steps in the mass distribution.

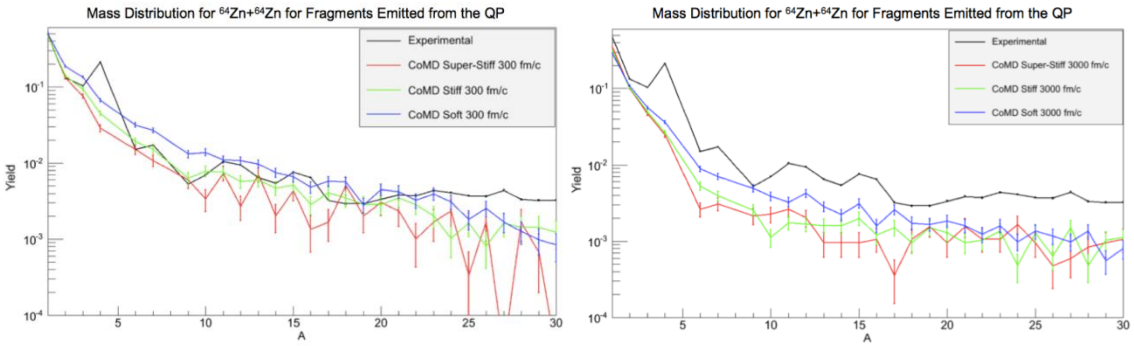

Figure 31. Mass distribution for fragments emitted from the QP for ^{64}Zn+^{64}Zn reactions from experimental data and CoMD simulations at 300 fm/c and 3000 fm/c.

The mass distributions for CoMD at 300 fm/c and 3000 fm/c and experimental data are shown in Figure 31. The CoMD distributions at 300 fm/c and 3000 fm/c peak at A=1 and the yield decreases with increasing mass. The CoMD at 300 fm/c agrees much better with the experimental data than the CoMD at 3000 fm/c. The CoMD at 300 fm/c matches the experimental distribution well over the entire mass range, except for alpha particles at A=4. The CoMD at 3000 fm/c matches the experimental values for LCP, but is lower than the experiment for much of the distribution. At both time-steps, there is a dependence on the asymmetry energy, which is shown in the ordering of the interactions, where the soft interaction has higher yields compared to the stiff and super-stiff interactions. The various interactions in the mass distribution for CoMD at 300 fm/c agree with the experimental distribution at various mass regions.

The charge and mass distributions show similar trends regarding the comparison of the AMD and CoMD simulations with the experimental results. The CoMD interactions show an asymmetry energy dependence in both distributions, while the AMD does not. Though the three interactions in CoMD are separated in the charge and mass distributions, none of them show better agreement with the experimental data than the others. The AMD and CoMD charge and mass distributions exhibit a dependence on the time-step of the simulation. For AMD and CoMD, the charge and mass distributions at the 300 fm/c time-step match closest to the experimental distribution, but there is no discernible interaction dependence.

3.8 QP Multiplicity Distributions

Total multiplicity distributions were also created for the fragments emitted from the QP. The results of the AMD simulations are shown in Figure 32. The experimental distribution peaks at a multiplicity of about 13. The AMD at 300 fm/c peaks around a multiplicity around 5 to 6, while the AMD at 300 fm/c with GEMINI and 3000 fm/c peak around a multiplicity of 18. The multiplicity distributions of AMD at 300 fm/c and 3000 fm/c are narrower than the multiplicity distribution of AMD at 300 fm/c with GEMINI, and are narrower than the experimental multiplicity distribution. This is different than the results from the inclusive data where the experimental distribution had a narrower width, similar to the AMD at 300 fm/c. The mean of the experimental distribution does not match the means of any of the AMD simulations shown, but instead lies in between them. There is no discernable interaction dependence, as the Gogny and Gogny-AS interactions produce similar results at each time-step.

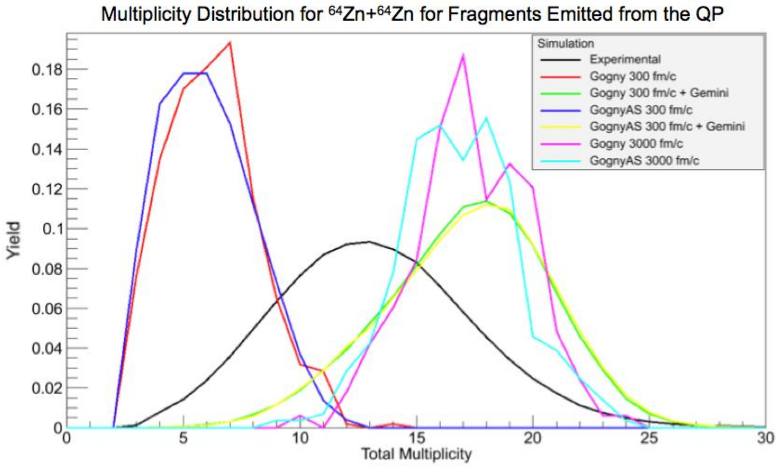

Figure 32. Multiplicity distribution for fragments emitted from the QP from ^{64}Zn+^{64}Zn reactions from experimental data and AMD simulations at 300 fm/c, 3000 fm/c, and 300 fm/c with GEMINI.

The multiplicity distributions for CoMD simulations at 300 fm/c and 3000 fm/c are shown in Figure 33. The CoMD at 300 fm/c has a peak in the multiplicity distribution around 5 for the super-stiff interaction. The stiff and soft interactions for CoMD at 300 fm/c have a less discernable peak and are fairly flat across a broad range of multiplicities. The CoMD at 3000 fm/c has an average multiplicity around 14 for the super-stiff interaction up to about 20 for the soft interaction. The peaks of the multiplicity distributions for both time-steps are much closer to the peak of the experimental distribution, compared to the inclusive data shown previously, but the experimental distribution average lies in between the two time-steps shown. The CoMD has a larger width in the multiplicity distributions than the experiment, but not nearly as wide as in the inclusive data. The dependence on the interaction is shown in the

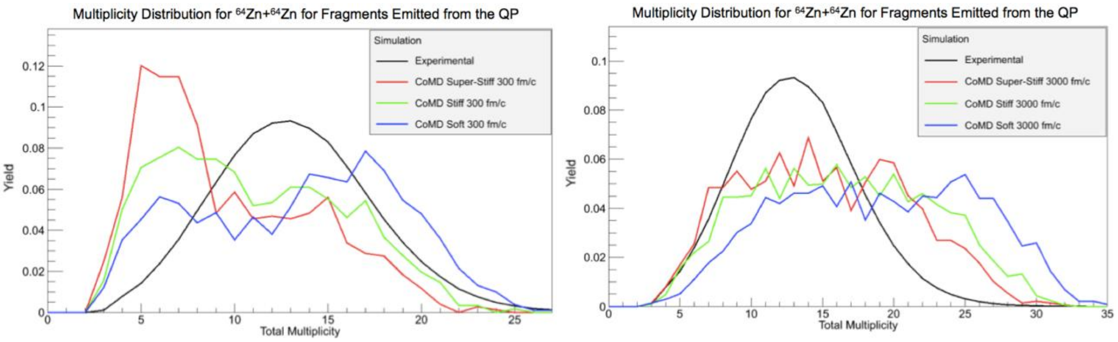

Figure 33. Multiplicity distribution for fragments emitted from the QP from ^{64}Zn+^{64}Zn reactions from experimental data and CoMD simulations at 300 fm/c and 3000 fm/c.

multiplicity distributions, where the super-stiff interaction has a lower average multiplicity than the soft interaction, but none of the interactions match the experimental multiplicity distribution better than the others.

The multiplicity of fragments emitted from the QP for the AMD and CoMD show similar trends in asymmetry energy and time-step as were seen in the inclusive data. All of the multiplicity distributions have narrower widths for fragments emitted from the QP compared to inclusive data. The peak of the experimental distribution does not agree with the peaks of the distributions for any of the time-steps shown, but instead lies in between the 300 fm/c and 3000 fm/c distributions for both the AMD and CoMD simulations. The AMD does not show an asymmetry energy dependence in the multiplicity distributions, while the CoMD shows an ordering in the interactions.

3.9 QP Isotope Distributions

Isotope distributions were constructed for fragments emitted from the QP for each of the AMD and CoMD simulations and experimental data. The relative yield of each isotope is plotted on the y-axis, calculated as the total isotope yield divided by the number of events. Isotope distributions for even numbered elements are shown in the top half of the figure, while isotope distributions for odd numbered elements are shown in the bottom half of the figure.

Figure 34 shows the time-step dependence of the isotope distribution for the AMD Gogny simulations at 300 fm/c, 3000 fm/c, and 300 fm/c with GEMINI. The Gogny interactions at 3000 fm/c and 300 fm/c with GEMINI have a higher relative yield

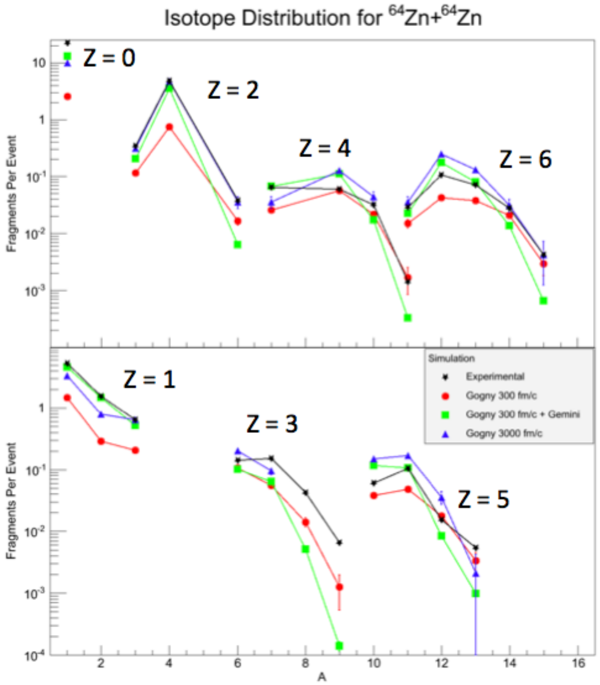

Figure 34. Isotope distributions for isotopes of elements Z=0 to Z=6 emitted from the QP for ^{64}Zn+^{64}Zn reactions from experiment and AMD Gogny simulations at 300 fm/c, 3000 fm/c and 300 fm/c with GEMINI.

for the most prominent isotope in each distribution. The simulations at later time-steps show the best agreement to the experimental isotope distributions for $Z \leq 6$.

The asymmetry energy dependence of the isotope distributions for the AMD simulation is shown in Figure 35. AMD Gogny and Gogny-AS simulations at 300 fm/c and 3000 fm/c are shown with the experimental isotope distributions. The difference between the Gogny and Gogny-AS interactions is most prevalent in the wings of the isotope distributions. For the most dominant isotopes, the two interactions have very similar yields. Neither of the interactions matches the experimental isotope distributions better than the other.

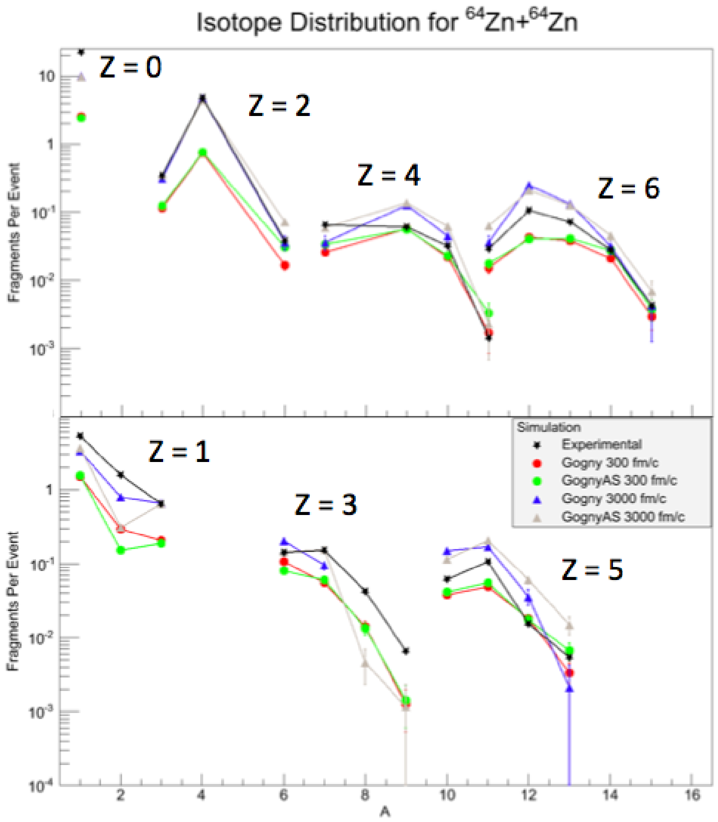

Figure 35. Isotope distributions for isotopes of elements Z=0 to Z=6 emitted from the QP for ^{64}Zn+^{64}Zn reactions from experiment and AMD Gogny and GognyAS simulations at 300 fm/c and 3000 fm/c.

Figure 36 shows the time-step dependence of the isotope distributions for the CoMD simulations. The stiff interaction is shown at 300 fm/c, 3000 fm/c, and 600 fm/c with GEMINI along with the experimental data. There is very little difference between the isotope distributions for the CoMD simulations at 300 fm/c and at 3000 fm/c. When GEMINI is added as an afterburner to the CoMD simulation, the overall yield and shape of the isotope distributions are very different, except for Z=3. For light isotopes and for even numbered elements, the CoMD with GEMINI agrees much better with the

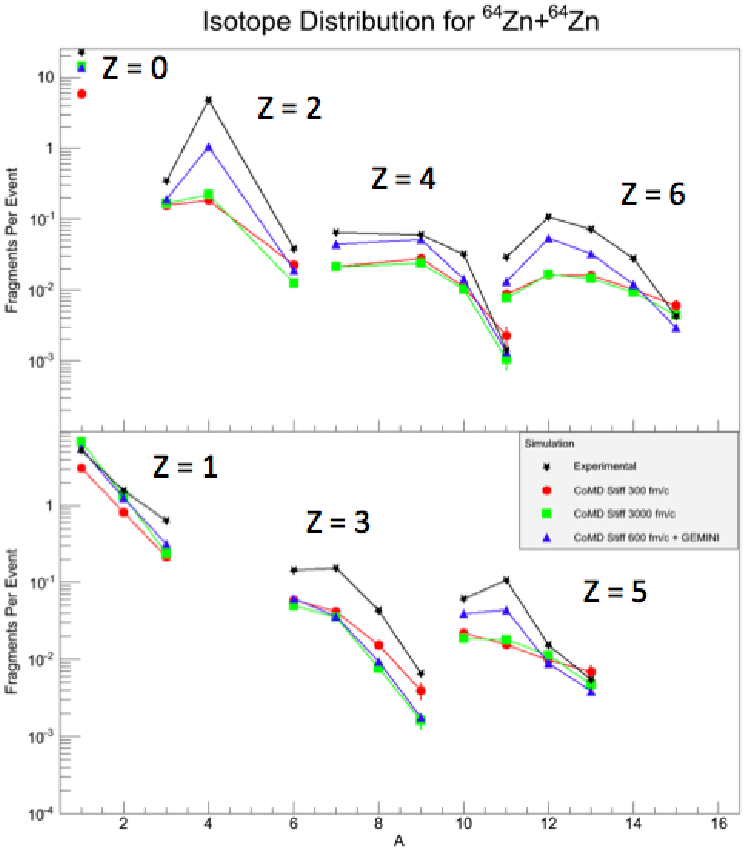

Figure 36. Isotope distributions for isotopes of elements Z=0 to Z=6 emitted from the QP for ^{64}Zn+^{64}Zn reactions from experiment and CoMD stiff simulations at 300 fm/c, 3000 fm/c and 600 fm/c with GEMINI.

experimental isotope distribution than the CoMD at 300 fm/c or 3000 fm/c. The largest change before and after the GEMINI model is in the most prominent isotope of each distribution, and there is less change in the wings of the distribution. The overall shape of isotope distributions from CoMD with GEMINI is closer to the shape of the experimental distribution.

The asymmetry energy dependence of the isotope distributions for CoMD is shown in Figure 37. The isotope distributions from the CoMD simulations of the soft, stiff, and super-stiff interactions at 3000 fm/c are shown along with the experimental isotope distributions. The soft interaction has a slightly higher yield than the stiff and super-stiff interactions, which is most notable for the most prominent isotope in each

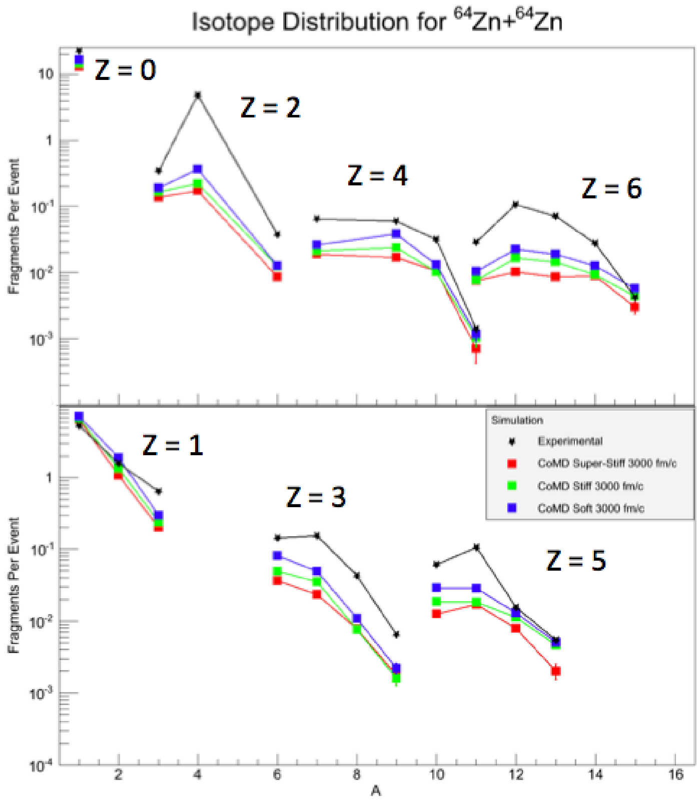

Figure 37. Isotope distributions for isotopes of elements Z=0 to Z=6 emitted from the QP for ^{64}Zn+^{64}Zn reactions from experiment and CoMD simulations at 3000 fm/c.

distribution. The three interactions have similar shapes, but the soft interaction has a higher overall yield and matches closer to the experiment. For almost every isotope in the plot, the CoMD soft interaction at 3000 fm/c agrees better with the experiment than the stiff or super-stiff interactions at 3000 fm/c.

The fragment distributions created from the reconstructed QP source show general agreement with the inclusive fragment distributions before the reconstruction. The longer time-steps in the AMD simulations match more closely to the fragment distributions overall. The CoMD also shows a large difference with the addition of GEMINI. The asymmetry energy difference is present in both models, but is much more pronounced in the CoMD model and in the wings of the isotope distributions.

3.10 QP Isoscaling

The isoscaling analysis can also be carried out on the fragments emitted from the reconstructed QP. In previous works [19], isoscaling has been performed on bins in N/Z of the QP instead of from system to system, as shown in the inclusive data. An N/Z distribution of the combined QP from each system is then produced and isoscaling is performed on bins selected in this distribution.

The N/Z distribution for reconstructed QP's from AMD and CoMD simulations along with the experimental data are shown in Figure 38. Both of these N/Z distributions were then divided into 5 bins, 0.06 units wide, stretching from 1.02 to 1.32 on the N/Z scale, such that bin 1 is from 1.02 to 1.08, bin 2 from 1.08 to 1.14, bin 3 from 1.14 to 1.20, bin 4 from 1.20 to 1.26, and bin 5 from 1.26 to 1.32. This includes as much of the distribution as possible, while also ensuring that each bin has good statistics for each model. When this N/Z distribution is divided into bins, the higher bins can be used as the neutron-rich sources and lower bins used as the neutron-poor sources for the isoscaling ratio.

Figure 39 shows isoscaling of Gogny at 300 fm/c with GEMINI for fragments emitted from the QP in bin 4 with the fragments emitted from the QP in bin 2. The

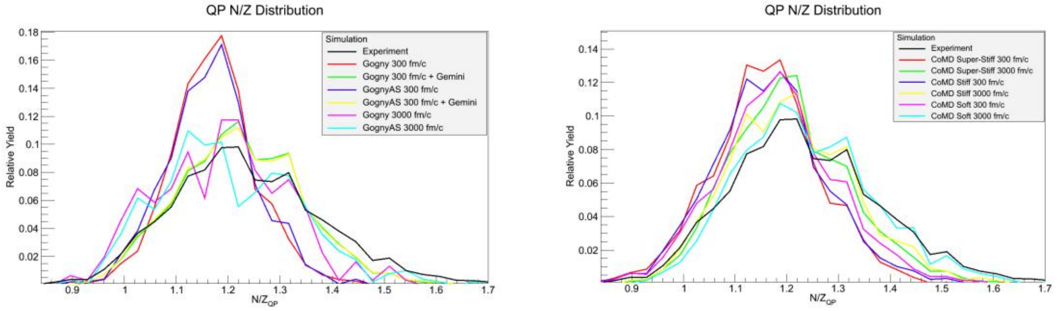

Figure 38. Neutron-to-proton, N/Z, distribution for reconstructed QP's from experimental data and results from AMD and CoMD simulations.

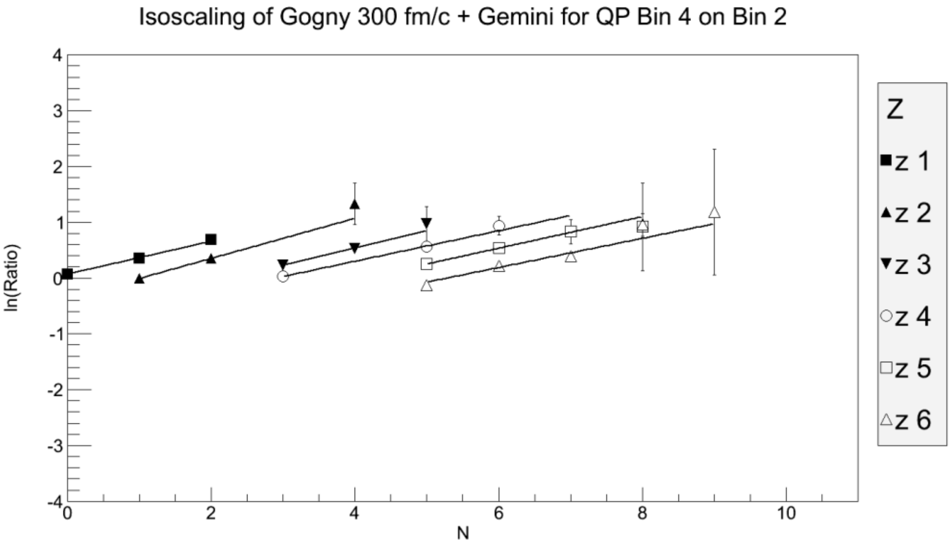

Figure 39. Isoscaling of bin 4 on bin 2 from the QP N/Z distribution for AMD Gogny at 300 fm/c with GEMINI.

isoscaling of QP fragments from bin 4 with bin 2 produces fits to the elements that are nearly parallel and evenly spaced. For isoscaling of fragments emitted from the QP, there must be at least 5 fragments in the event. This is lower than the limit of 15 placed on non-reconstructed fragment yields due to the reduction in events and fragments after the reconstruction. This lower yield also results in larger error bars in the isoscaling calculations.

A global fit of α and β can be produced from the results of the QP isoscaling, similar to the one used in the system-to-system isoscaling. The global α parameter fit is shown in addition to the individual α of each element in the plot of α vs. Z in Figure 40 for bin 4 on bin 2 for Gogny at 300 fm/c with GEMINI.

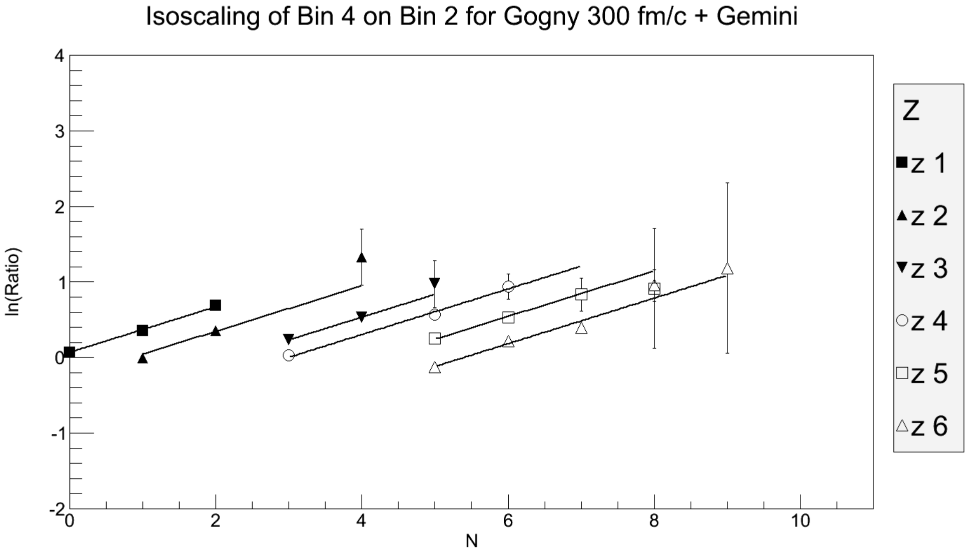

Figure 40. Isoscaling parameter α vs. Z for bin 4 on bin 2 for AMD Gogny at 300 fm/c with GEMINI with individual α parameters (points) and global α parameter (line), 0.17.

The global α value shows fairly good agreement to the individual α values from the isoscaling of bin 4 and bin 2 for Gogny at 300 fm/c with GEMINI for low Z values, except for Z=3. Changing the bins used in isoscaling changes the Δ value, which affects the α value, just as changing the systems in system-to-system isoscaling changes the α value. Figure 41 shows the global α for isoscaling of bin 5 with bins 1 through 4. This provides four different combinations of bin differences to show how changing the difference between the bins used in isoscaling affects the value of α.

The closer the bins are to each other, the lower the Δ value and α value are, since the sources have a closer neutron-to-proton ratio for closer bins. The global α fits the individual α values fairly well across each of the isoscaling bin combinations. From these bin combinations, the Δ can be calculated. The Δ value for bin-to-bin isoscaling is calculated in a similar fashion as before with the system-to-system isoscaling. Instead of finding a (Z/A) for each system, a distribution of the total (Z/A) for all of the fragments in each event for each bin is created for the fragments emitted from the QP. The mean of this distribution is then squared and used in the Δ calculation.

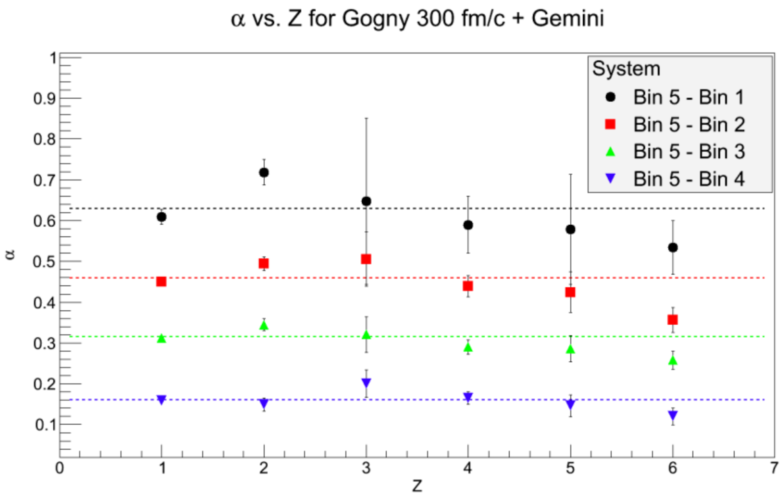

Figure 41. Isoscaling parameter α vs. *Z* for bin 5 on bin 1, bin 2, bin 3, and bin 4 for AMD Gogny at 300 fm/c with GEMINI.

Comparisons of α vs Δ can be studied in the same way as the inclusive data, now using the bin-to-bin isoscaling. Figure 42 shows the α vs Δ for each of the simulations and experiment for the bin 5 to bin 2 isoscaling.

The simulation lines are fit in the same way as before, using a linear fit to each point from the bin-to-bin isoscaling of the simulation and forcing the fit through the origin. In the plot of α vs. Δ for bin 5 on bin 2, the simulation results for AMD at 300

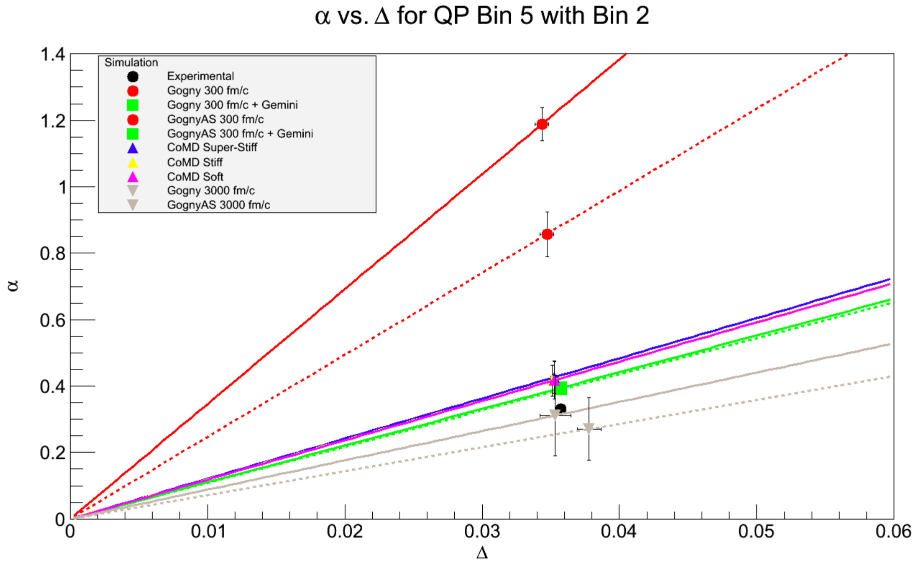

Figure 42. Isoscaling parameter α vs. Δ for bin 5 on bin 2 for fragments from the reconstructed QP.

fm/c show a clear distinction from the rest of the simulation results at 3000 fm/c and 300 fm/c with GEMINI. The AMD Gogny and Gogny-AS at 300 fm/c have a larger α than the experimental data and the rest of the simulations, but have similar Δ and similar ordering of the soft Gogny interaction above the stiff Gogny-AS interaction. The different models in the CoMD simulation do not show an ordering from soft to stiff, which is mainly due to the large error bars in the global α calculation and the close proximity of the α values. The AMD at 3000 fm/c now have the lowest α value of the simulations, and the AMD with GEMINI have the second lowest. The AMD at 3000 fm/c shows the same ordering of the soft Gogny interaction above the stiffer Gogny-AS interaction. With the QP isoscaling, the experimental point now lies nearly on the line for the Gogny interaction at 3000 fm/c and is also within error bars of the Gogny-AS interaction at 3000 fm/c. The proximity of the experimental point to each of the 3000 fm/c simulations and the 300 fm/c with GEMINI shows the importance of the time-step of the simulation and the analysis of a cooled system.

Figure 43 combines all of the possible bin-to-bin isoscaling values onto one figure for the experimental data and simulations. The experimental data in black circles are grouped according to the difference in the bins. There are four points at the lowest Δ value, corresponding to the isoscaling of adjacent bins. The experimental points are then aligned in groups of three, two, and one which correspond to two bins apart, three bins apart, and four bins apart. The same bin combinations have been used for each of the simulations, but the individual points are not shown. The lines are fits to the all of the ten data points for each of the simulations and forced through the origin. The Gogny and Gogny-AS interactions at 300 fm/c are close together. The AMD at 300 fm/c and the AMD Gogny interaction at 3000 fm/c are separate from the rest of the simulations. The AMD at 300 fm/c with GEMINI, AMD Gogny-AS at 3000 fm/c, and CoMD at 3000 fm/c are all very close together and almost lie on top of each other. The experimental

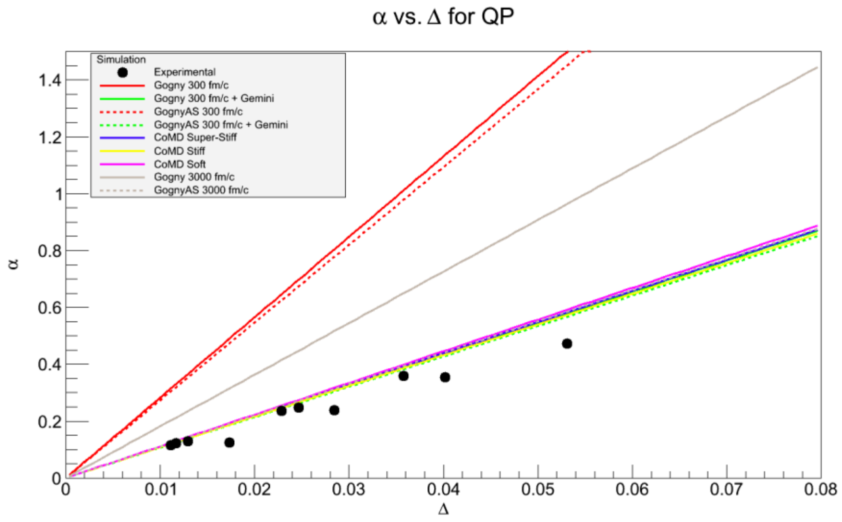

Figure 43. Isoscaling parameter α vs. Δ for all bin combinations for fragments from the reconstructed QP.

data lie very close to the simulations at later time-steps, except for the Gogny interaction at 3000 fm/c. The lines are the average fit to the data, and the error bars are taken into consideration when fitting the data. As shown in Figure 42, the error bars overlap across several of the simulations, so there is no statistical certainty on the agreement of the data with a specific interaction. Though a claim to the asymmetry energy is not valid, the dependence on the time-step of the interaction is shown to be very important in the isoscaling analysis in the AMD simulations.

The α values for simulations of AMD and CoMD from the reconstructed QP were studied with respect to the time-step of the simulation. Figure 44 shows the isoscaling values from bin 5 on bin 2 for multiple simulations up to a time of 3000 fm/c. The results for AMD at 300 fm/c with GEMINI and experimental data are plotted at 3000 fm/c to observe the final results of each simulation. As before in the system-to-system isoscaling, the effect of time can be seen on the isoscaling parameter α as it decreases with the length of the simulation. The CoMD simulation shows a small

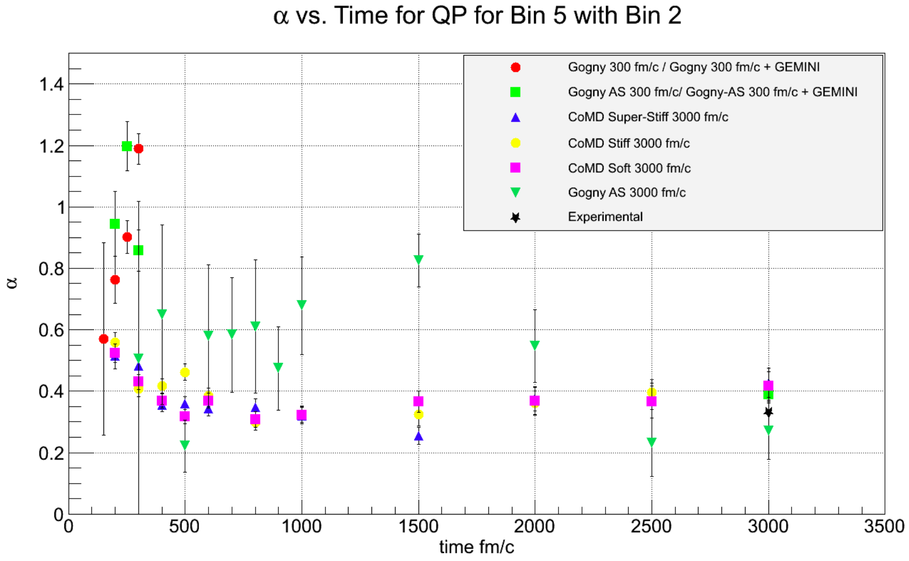

Figure 44. Isoscaling parameter α vs. time for bin 5 on bin 2 for fragments from the reconstructed QP. AMD at 300 fm/c with GEMINI and experimental data are shown at 3000 fm/c.

decrease in the α value with time for each of the interactions, but the change is slight. The AMD shows a very large dependence on the time-step of the simulation, which can be seen in the difference between the results at 300 fm/c and at 3000 fm/c. Only the Gogny-AS interaction is shown to 3000 fm/c due to the low statistics for the Gogny interaction. The Gogny-AS also has large error bars due to low statistics, but the trend in α over time is still evident. The AMD at 300 fm/c with GEMINI and the CoMD at 3000 fm/c each have a larger α value than the experimental data and have small error bars that do not overlap with the experimental point. The α value for AMD Gogny-AS at 3000 fm/c is below the experimental point, but the experimental α value is within the error bars.

In the isoscaling results, there is a clear trend on the dependence of the time-step of the simulation and the comparison to experimental data in the plots of α vs. Δ. In the inclusive data, this was evident as well, but the experiment did not agree with a specific simulation. In the QP isoscaling, the experimental data lies very close to the simulations at 3000 fm/c and with GEMINI. The QP isoscaling shows a very good agreement with the experiment, but only with the longer time-steps and including statistical de-excitation. An important observation is the lack of dependence on the type of de-excitation in the AMD simulation. In Figure 43, the fits for AMD with GEMINI and AMD Gogny at 3000 fm/c lie directly on top of each other. This shows that the results from isoscaling do not depend on whether the AMD is de-excited dynamically to 3000 fm/c or statistically with the GEMINI model at 300 fm/c.

3.11 Comparison to Previous Work

The linear relationship between α and Δ has been shown in this work and in previous works using AMD [18] and experimental data [20]. In Figure 6 in the introduction, comparisons between these two works are shown. In this comparison, there are multiple event selections. The α from the AMD simulation is calculated for central collisions and includes all fragment types [18]. The α from the experiment includes only fragments detected at 44° in lab and with a charge of $3 \leq Z \leq 7$ [20]. The Δ from the AMD simulation includes central events and only fragments with A>4 [18]. The Δ used in Shetty et al. [20] is extrapolated from comparing the initial $(Z/A)^2$ with the $(Z/A)^2$ at 300 fm/c from previous AMD simulations.

Various event selections have been used when calculating α and Δ values and comparing between models and experiment. Tables 1-7 shows various calculations of α, Δ, and $(Z/A)^2$ using previously discussed event selections and new event selections. For the initial system, $(Z/A)^2$ and Δ values are calculated from the charge and mass of the target and projectile. The subscript "sys" will be used to denote the initial system values. The subscript "Total" is used for inclusive data, over all impact parameters and for all fragments. The $(Z/A)^2$ and Δ values from simulation results were also studied at central impact parameters and only including fragments with A>4. This event selection applies the same cuts to the simulation results from this work that were used in the AMD simulations by Ono et al. [18]. This cut will be denoted by the subscript "A>4". In the results presented by Ono et al. [18], the simulation is not filtered, and the simulation data here will be presented also as unfiltered only for the "A>4" event selection. The α and Δ values from the isoscaling of reconstructed QP are shown as well. For the QP values, the event selection is inclusive due to fewer events. These will be denoted by the subscript "QP". In order to approximate the α values from the experiment by Shetty et al. [20], α was extracted from isoscaling of fragments detected within the angular range of Ring 9, 35.8° to 45.0°, and with a charge of $3 \leq Z \leq 7$. This event selection will be denoted with the subscript "Ring 9". The Δ values used in Shetty et al. [20] are extrapolated from the AMD results by Ono et al. [18], by comparing the initial $(Z/A)^2$ of the system to fit to the $(Z/A)^2$ values from AMD at 300 fm/c [18].

Figure 45 shows the plot used to extrapolate $(Z/A)^2$ values by Shetty et al. [20]. By using the initial system $(Z/A)^2$ values of the reactions from this work, values of $(Z/A)^2$ for AMD simulations at 300 fm/c can be extracted in the same manner as the $(Z/A)^2$ values in Shetty et al. [20]. These Δ values are denoted as "extrapolated". For experimental extrapolated $(Z/A)^2$ values, the average of the Gogny and Gogny-AS values extrapolated from the AMD at 300 fm/c are used.

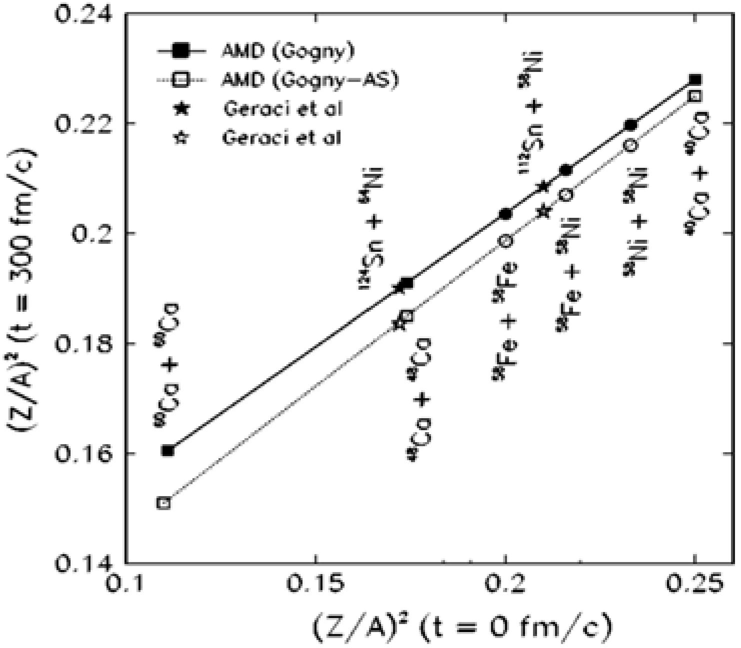

Figure 45. $(Z/A)^2$ of the initial system at t=0 fm/c is plotted against $(Z/A)^2$ of the system from AMD simulations at t=300 fm/c. The lines are fits to the ^{60}Ca+^{60}Ca, ^{48}Ca+^{48}Ca, and ^{40}Ca+^{40}Ca reactions. The rest of the reactions are plotted according to their initial $(Z/A)^2$. The figure is adapted from [20].

Experiment			
$(Z/A)^2$	^{70}Zn+^{70}Zn	^{64}Ni+^{64}Ni	^{64}Zn+^{64}Zn
System	0.184	0.191	0.220
Extrapolated	0.193	0.196	0.211
Total	0.047	0.054	0.070
A>4	0.212	0.215	0.220
QP	0.150	0.159	0.181

Δ	^{70}Zn/^{64}Ni	^{64}Ni/^{64}Zn	^{70}Zn/^{64}Zn
System	0.007	0.028	0.036
Extrapolated	0.003	0.015	0.018
Total	0.007	0.016	0.023
A>4	0.003	0.005	0.007
QP	0.010	0.021	0.031

α	^{70}Zn/^{64}Ni	^{64}Ni/^{64}Zn	^{70}Zn/^{64}Zn
Total	0.075	0.322	0.400
Ring 9	0.095	0.211	0.314
QP	0.082	0.321	0.406

Table 1. Values of $(Z/A)^2$, Δ, and α for various event cuts on the experiment. See the main text for an explanation of terms.

AMD Gogny 300 fm/c			
$(Z/A)^2$	^{70}Zn+^{70}Zn	^{64}Ni+^{64}Ni	^{64}Zn+^{64}Zn
System	0.184	0.191	0.220
Extrapolated	0.196	0.199	0.213
Total	0.150	0.161	0.185
A>4	0.210	0.208	0.212
A>4 Unfiltered	0.191	0.196	0.218
QP	0.190	0.198	0.214

Δ	^{70}Zn/^{64}Ni	^{64}Ni/^{64}Zn	^{70}Zn/^{64}Zn
System	0.008	0.028	0.036
Extrapolated	0.003	0.014	0.017
Total	0.011	0.024	0.034
A>4	-0.002	0.004	0.002
A>4 Unfiltered	0.006	0.021	0.027
QP	0.007	0.017	0.024

α	^{70}Zn/^{64}Ni	^{64}Ni/^{64}Zn	^{70}Zn/^{64}Zn
Total	0.133	0.428	0.570
QP	0.039	0.513	0.559

Table 2. Values of $(Z/A)^2$, Δ, and α for various event cuts on the AMD Gogny simulation at 300 fm/c. See the main text for an explanation of terms.

AMD Gogny-AS 300 fm/c			
$(Z/A)^2$	^{70}Zn+^{70}Zn	^{64}Ni+^{64}Ni	^{64}Zn+^{64}Zn
System	0.184	0.191	0.220
Extrapolated	0.190	0.194	0.209
Total	0.153	0.163	0.187
A>4	0.207	0.210	0.212
A>4 Unfiltered	0.188	0.195	0.216
QP	0.194	0.197	0.215

Δ	^{70}Zn/^{64}Ni	^{64}Ni/^{64}Zn	^{70}Zn/^{64}Zn
System	0.008	0.028	0.036
Extrapolated	0.004	0.015	0.019
Total	0.010	0.024	0.034
A>4	0.002	0.002	0.005
A>4 Unfiltered	0.006	0.022	0.028
QP	0.004	0.018	0.021

α	^{70}Zn/^{64}Ni	^{64}Ni/^{64}Zn	^{70}Zn/^{64}Zn
Total	0.122	0.362	0.499
QP	0.114	0.567	0.581

Table 3. Values of $(Z/A)^2$, Δ, and α for various event cuts on the AMD Gogny-AS simulation at 300 fm/c. See the main text for an explanation of terms.

Gogny 300+GEMINI			
$(Z/A)^2$	^{70}Zn+^{70}Zn	^{64}Ni+^{64}Ni	^{64}Zn+^{64}Zn
System	0.184	0.191	0.220
Extrapolated	0.196	0.199	0.213
Total	0.022	0.026	0.036
A>4	0.212	0.213	0.217
A>4 Unfiltered	0.223	0.224	0.228
QP	0.146	0.156	0.184

Δ	^{70}Zn/^{64}Ni	^{64}Ni/^{64}Zn	^{70}Zn/^{64}Zn
System	0.008	0.028	0.036
Extrapolated	0.003	0.014	0.017
Total	0.004	0.010	0.0140
A>4	0.001	0.003	0.004
A>4 Unfiltered	0.002	0.004	0.006
QP	0.010	0.028	0.037

α	^{70}Zn/^{64}Ni	^{64}Ni/^{64}Zn	^{70}Zn/^{64}Zn
Inclusive	0.071	0.267	0.336
QP	0.062	0.261	0.316

Table 4. Values of $(Z/A)^2$, Δ, and α for various event cuts on the AMD Gogny simulation at 300 fm/c with GEMINI. See the main text for an explanation of terms.

GognyAS 300+GEMINI			
$(Z/A)^2$	^{70}Zn+^{70}Zn	^{64}Ni+^{64}Ni	^{64}Zn+^{64}Zn
System	0.184	0.191	0.220
Extrapolated	0.190	0.194	0.209
Total	0.021	0.025	0.035
A>4	0.212	0.213	0.217
A>4 Unfiltered	0.223	0.224	0.228
QP	0.146	0.156	0.183

Δ	^{70}Zn/^{64}Ni	^{64}Ni/^{64}Zn	^{70}Zn/^{64}Zn
System	0.008	0.028	0.036
Extrapolated	0.004	0.015	0.019
Total	0.004	0.010	0.014
A>4	0.001	0.004	0.004
A>4 Unfiltered	0.001	0.004	0.006
QP	0.010	0.028	0.037

α	^{70}Zn/^{64}Ni	^{64}Ni/^{64}Zn	^{70}Zn/^{64}Zn
Inclusive	0.072	0.261	0.329
QP	0.066	0.253	0.316

Table 5. Values of $(Z/A)^2$, Δ, and α for various event cuts on the AMD Gogny-AS simulation at 300 fm/c with GEMINI. See the main text for an explanation of terms.

Gogny 3000		
$(Z/A)^2$	^{70}Zn+^{70}Zn	^{64}Zn+^{64}Zn
System	0.184	0.220
Extrapolated	0.196	0.213
Total	0.021	0.038
A>4	0.204	0.211
A>4 Unfiltered	0.214	0.224
QP	0.155	0.192

Δ	^{70}Zn/^{64}Zn
System	0.036
Extrapolated	0.017
Total	0.017
A>4	0.007
A>4 Unfiltered	0.010
QP	0.037

α	^{70}Zn/^{64}Zn
Inclusive	0.440
QP	0.209

Table 6. Values of $(Z/A)^2$, Δ, and α for various event cuts on the AMD Gogny simulation at 3000 fm/c. See the main text for an explanation of terms.

GognyAS 3000		
$(Z/A)^2$	^{70}Zn+^{70}Zn	^{64}Zn+^{64}Zn
System	0.184	0.220
Extrapolated	0.190	0.209
Total	0.021	0.039
A>4	0.198	0.207
A>4 Unfiltered	0.209	0.218
QP	0.151	0.190

Δ	^{70}Zn/^{64}Zn
System	0.036
Extrapolated	0.019
Total	0.018
A>4	0.008
A>4 Unfiltered	0.009
QP	0.039

α	^{70}Zn/^{64}Zn
Inclusive	0.347
QP	0.354

Table 7. Values of $(Z/A)^2$, Δ, and α for various event cuts on the AMD Gogny-AS simulation at 3000 fm/c. See the main text for an explanation of terms.

Several observations can be made for the values in Tables 1-7, specifically in the values of $(Z/A)^2$. In the experimental data, the $(Z/A)^2$ of the system, extrapolated, and A>4 calculations, have very similar values, while the total and QP have lower values. This can be explained by the addition of free neutrons in the calculations of the total and

QP $(Z/A)^2$ which are not included in the other calculations, which increases the A but not the Z, lowering the $(Z/A)^2$ value. This trend of lower total and QP $(Z/A)^2$ values is not present in the AMD simulations at 300 fm/c, but shows up in the AMD at 3000 fm/c and at 300 fm/c with GEMINI. The lack of the lower values in the AMD at 300 fm/c suggests that there are fewer free neutrons at this early stage of AMD than in the experiment and AMD at 3000 fm/c and at 300 fm/c with GEMINI. This also shows the similarities between the AMD at longer time-steps and the experiment as compared to the AMD at shorter time-steps.

The importance of studying the α and Δ values for different event selections is for comparison to previous data. Treating the data from this work in the same manner as previous results allows for a direct comparison. The experimental results in this work are studied is the same manner as the experimental results by Shetty et al. [20]. These are then included in the comparison to AMD results by Ono et al. [18].

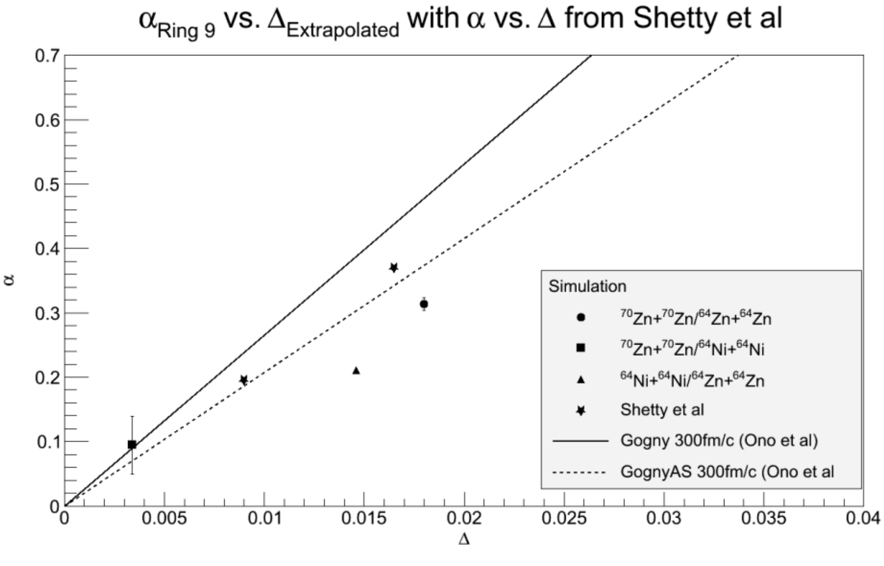

Figure 46. Plot of α_{Ring9} vs. $\Delta_{extrapolated}$ from experimental results in this work added to the AMD simulations [18] and experimental results from Shetty et al. [20].

Figure 46 analyzes the experimental results in this work in the same way as the experimental results in Shetty et al. [20]. The α_{Ring9} value approximates the single telescope from Shetty et al., and the $\Delta_{extrapolated}$ is calculated from $(Z/A)^2$ values in the same way and from the same figure as $(Z/A)^2$ values from Shetty et al. This offers the most direct comparison of the current experimental results and the previous experimental results using the same event selection. The AMD Gogny and Gogny-AS simulation results at 300 fm/c shown in Figure 46 are from previous simulations that have been compared to experimental data [18,20]. The conclusion drawn by Shetty et al. in their analysis was that the experiment agrees most closely with the stiff Gogny-AS definition of the asymmetry energy from AMD simulations at 300 fm/c. The results from the experimental data in this work agree with the previous results and correspond most closely with the Gogny-AS line from AMD.

Instead of using AMD results from previous work, the AMD simulations of the reactions in this work were also studied and compared to the experimental data in the same manner as before.

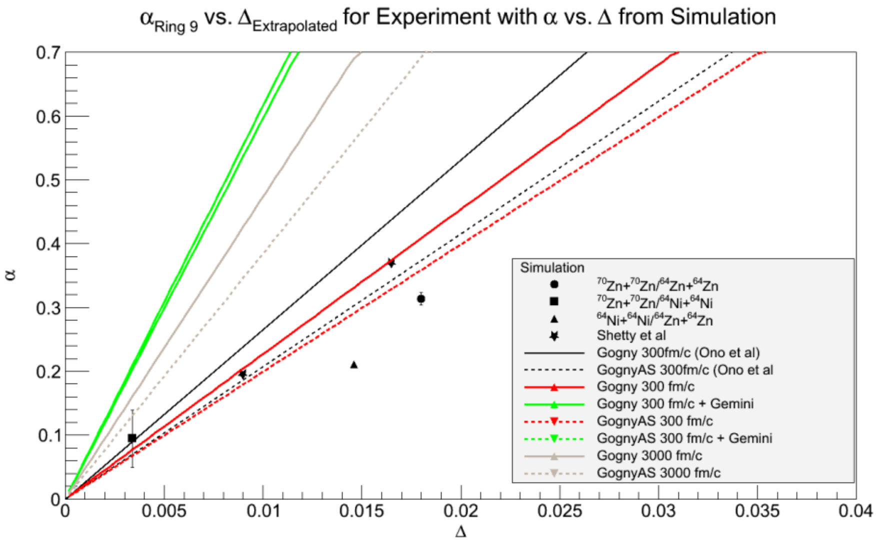

Figure 47. Plot of α_{Ring9} vs. $\Delta_{extrapolated}$ from the experimental results and α_{Total} vs. $\Delta_{A>4,unfiltered}$ from AMD simulations at 300 fm/c, 3000 fm/c, and 300 fm/c wth GEMINI.

Figure 47 shows the AMD simulations at 300 fm/c, 300 fm/c with GEMINI, and 3000 fm/c for all three isoscaling systems added to the lines and points from Figure 46. Event cuts are applied to the AMD results to include the α_{Total} and $\Delta_{A>4,\text{unfiltered}}$ to best match the AMD results from Ono et al. [18]. The AMD simulations from this work match fairly well to the AMD results from Ono et al. [18], which shows consistency in the model across various reactions. The differences between the two simulations can be attributed to the different reactions that are modeled, and the different types of model, where Ono et al. used AMD-V [18] and AMD-DS was used in this work. The AMD at longer time-steps has a lower $\Delta_{A>4,\text{unfiltered}}$ value than the AMD at 300 fm/c, which means that the $(Z/A)^2$ of the reactions at the longer time-steps are very similar compared to the $(Z/A)^2$ at 300 fm/c. The experiment corresponds more closely to the AMD simulations at 300 fm/c than at 3000 fm/c and 300 fm/c with GEMINI, and the experimental data from this work is still more closely aligned with the Gogny-AS interaction.

3.12 Excitation Energy

Throughout the isoscaling and fragment distributions, the dependence on the time-step of the interaction, and the addition of GEMINI has been shown to be important to the agreement of the simulations and experimental data. The AMD and CoMD simulations are dynamical and evolve over time. The target and projectile collide and separate and are excited and proceed to de-excite by particle emission and fragmentation. Analyzing the simulation at 300 fm/c provides a different picture of the fragmentation than at 3000 fm/c. At 300 fm/c, the system has not de-excited completely and usually has some excited fragments left, but by 3000 fm/c, the system is often considered cooled and should have very little excitation energy left. When GEMINI is applied to the simulation, it de-excites the fragments to zero excitation energy. In the dynamical model, stopping the simulation at 3000 fm/c does not always ensure zero excitation energy. Figure 48 shows a plot of the excitation energy over time for unfiltered results of the reaction of ^{64}Zn+^{64}Zn from simulations of AMD Gogny and Gogny-AS and CoMD soft, stiff, and super-stiff.

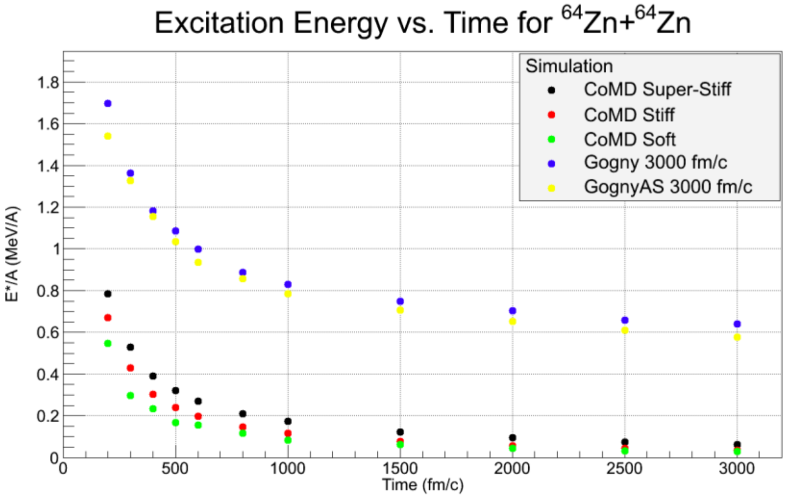

Figure 48. Excitation energy of all of the fragments from ^{64}Zn+^{64}Zn for unfiltered results from AMD and CoMD.

The excitation energy for each of the interactions decreases over time. This is expected as the excited system undergoes fragmentation and particle emission to de-excite. The results of the CoMD model behave as expected, beginning with an excited system that de-excites over time until there is little to no excitation energy left at 3000 fm/c. This means that the results of the CoMD that are studied above at 3000 fm/c are from a cooled system. The excitation energy of AMD does not follow the expected path of de-excitation in the system. The simulation begins with higher excitation energy than the CoMD, and decreases as the system fragments and de-excites, but instead of de-exciting to zero, the AMD results seem to level off. The AMD at 3000 fm/c still has some excitation energy left in the system, and it is not clear from this plot, if the excitation energy ever goes to zero. The AMD at 3000 fm/c agreed with many of the experimental results in the distributions and isoscaling, but there was a clear difference between results from AMD at 3000 fm/c and results with GEMINI. This is due to the difference in the excitation energy still present in the system at 3000 fm/c and the lack of excitation energy after GEMINI. Even with the difference in excitation energy for AMD at 3000 fm/c, the QP isoscaling results still show agreement with the AMD at 3000 fm/c, suggesting that the excitation energy does not affect the fragment distributions. The excitation energy in the system should have an impact on the fragment distributions, but the results from the models shown above do not show this dependence. The AMD at 3000 fm/c agreed fairly well with the experimental data throughout the results. The excitation energy in the AMD does not seem to greatly affect the fragment production of the simulation or its use in comparing to experimental results.

CHAPTER IV
CONCLUSIONS

Understanding the nuclear EoS is an important goal in the field of nuclear science. The EoS for asymmetric nuclear matter is important for the understanding of neutron stars, supernovae, and nuclear structure. Probing the E_{sym} term in the EoS allows for the study of asymmetric nuclear matter and constraining the asymmetry energy can provide a better understanding of nuclear matter. Many theoretical models use various forms of the asymmetry energy to describe the interaction of nuclei. Results of fragment distributions and isoscaling have been shown from the multiple interactions described by AMD and CoMD. These results show a dependence not only on the form of the asymmetry energy, but also on the time-step of the simulation. The effect of the statistical model GEMINI, when used as an afterburner for AMD is also shown.

The different time-steps in the AMD and CoMD simulations provide different results when studying fragment distributions and isoscaling. The effect of the time-step of the simulation is shown not only in the differences between results at 300 fm/c and 3000 fm/c, but also when adding GEMINI as an afterburner to the dynamical simulations. For charge, mass, and multiplicity distributions, the simulations at 3000 fm/c and with GEMINI agree fairly well with each other, even though they may not have agreed with the data at times, such as in Figure 32. The distributions often have similar shapes and relative yields. This can be attributed to the fragments in both systems being fully de-excited. This does not hold true in the isotope distributions, where the addition of GEMINI often yields a higher relative yield, especially for the most prominent isotope. The importance of studying the different time-steps is also important in the isoscaling analysis. The AMD at 300 fm/c was often separated from the AMD at 3000 fm/c and 300 fm/c with GEMINI. These later time-steps from AMD were close together and often grouped well with the CoMD at 3000 fm/c. The dependence of isoscaling on the time-step was very evident not only in the plots of α vs Δ, but also in the plot of α vs. time. The α value from AMD at 3000 fm/c and 300 fm/c with GEMINI agreed very well with the experiment. This shows how the isoscaling changes over time and the importance of studying isoscaling at multiple time-steps. An important result from the analysis of isoscaling was the agreement between the AMD at 3000 fm/c and at 300 fm/c with GEMINI. The α values for these two time-steps were very close together, which shows that the type of de-excitation is not as important in the study of isoscaling. De-excitation over time using a dynamical simulation provided the same final result as de-excitation using a statistical decay model from an earlier time-step.

The AMD and CoMD models have several interactions with various asymmetry energy values. These interactions were highlighted in some of the analyses. The AMD Gogny and Gogny-AS interactions showed the greatest difference in the isoscaling analysis. In the fragment distributions, there was very little difference between the two interactions as the Gogny and Gogny-AS provided very similar results. In the isoscaling analysis, the α values and the lines from the α vs. Δ plots always showed a separation. In the isoscaling, the alpha value for the soft Gogny interaction was always higher than the stiffer Gogny-AS interaction. This was true for AMD at 300 fm/c, 3000 fm/c, and 300 fm/c with GEMINI. In CoMD, the soft, stiff, and super-stiff interactions showed a difference in almost every analysis. For each of the fragment distributions, there was an ordering to the interactions from soft to super-stiff. The fragment distributions were more sensitive to the three interactions in CoMD, than they were to the Gogny and Gogny-AS interactions. The CoMD interactions were also separated in the isoscaling analysis, though not as clearly as the AMD simulations. The α values of the three CoMD interactions were fairly close together and there was not a large enough difference to confidently distinguish between the interactions. For various analyses, the differences in the interactions in the AMD and CoMD simulations were shown, but rarely were the differences large enough to make conclusive statements about the asymmetry energy dependence.

The fragment distributions and isoscaling analysis were studied for fragments from the entire system, as well as for fragments from a reconstructed QP. Studying the fragments emitted from the QP allowed for the study of a single source of the fragmentation instead of multiple sources. The results of the fragment distributions for fragments from the reconstructed QP were mostly similar to the inclusive results. The biggest difference came in the multiplicity distributions, where the multiplicity of the experimental data was between the simulation results at 300 fm/c and 3000 fm/c for the AMD and CoMD simulations. The multiplicity distributions for fragments emitted from the QP were also much narrower, which is mostly due to having a single smaller source instead of the entire system. The isoscaling analysis also provided an interesting result in comparison to the inclusive data. In the QP isoscaling, the lines of α vs Δ for AMD at 3000 fm/c and 300 fm/c with GEMINI, and the CoMD at 3000 fm/c, lie on top of each other, with the AMD at 300 fm/c separate from the rest of the simulations. The QP isoscaling shows the large dependence on the time-step of the simulation in the analysis. It also shows less of a difference between the AMD and CoMD simulations, as both provide a very similar α value at 3000 fm/c.

Each of the simulations was compared to experimental data in fragment distributions and the isoscaling analysis. The dependence on the time-step of the simulation and the asymmetry energy of the interaction was shown to affect the agreement of the simulation with the experimental data. In the charge and mass distributions, the time-step of the simulation had a larger effect than the asymmetry energy for the AMD and CoMD results. The AMD and CoMD at 300 fm/c generally had the better agreement with the experimental data over the entire charge and mass range, although this was not exclusively the case, especially for LCP. For the multiplicity distributions, the time-step of the simulation had a larger effect than the asymmetry energy. The multiplicity distributions for the AMD and CoMD simulations at 300 fm/c agreed fairly well with the experimental data. There was not a clear indication of one interaction agreeing more closely with the experimental data than another interaction in the multiplicity distributions. In the isotope distributions, both the time-step and asymmetry energy had an effect on the agreement of the simulations with the experimental data. In the inclusive data, the AMD and CoMD at 3000 fm/c and with GEMINI added provided a better match to the experimental isotope distributions than the AMD and CoMD at 300 fm/c. There were few differences in the various interactions in the isotope distributions, and most of these were observed in the wings of the isotope distributions. In the isotope distributions from the reconstructed QP, the simulations at later time-steps provided a better agreement with the experimental data as well. In the CoMD at 3000 fm/c, the effect of the asymmetry energy in the isotope distributions was important also, as the soft interaction agreed better with the experimental data than the stiff or super-stiff interactions. In the isoscaling analysis for inclusive data, the experiment did not provide a better agreement with a specific simulation or time-step in the α vs Δ plots. In the isoscaling from the reconstructed QP, the experimental data clearly matched the simulations at later time-steps, as shown in the α vs Δ plots. This agreement with longer time-steps shown in the α vs Δ figures was much clearer with the inclusion of the QP reconstruction. The α vs time figures exhibited a much clearer dependence of isoscaling on the time-step of the simulation. The experimental data agreed very well with the AMD at later time-steps in the inclusive data. In the reconstructed QP isoscaling, the α values agreed very well for all of the simulations at the later time-step.

The experimental data in this work was also compared with previous work. To provide a proper comparison with previous work, various event selections were applied to the simulations and experiment in this work. The results showed that the experimental data agrees most closely with the AMD Gogny-AS interaction at 300 fm/c, using the cuts from previous works. This agrees with previous results [20], which shows consistency in the isoscaling analysis. This disagrees with the previous assertion that the isoscaling of the experiment agrees better with the simulations at longer time-steps, but this comparison relies on different event selections and not the complete data.

This work highlights the use of dynamical and statistical simulations in the study of fragment distributions and isoscaling in comparison to experimental data. The different analyses showed a dependence on the time-step of the simulation and the asymmetry energy of the interaction. When comparing the experimental data to the simulations, multiple conclusions can be drawn about which asymmetry energy and time-step agrees most closely with the experimental data. In the fragment distributions, there is no large asymmetry energy dependence shown, and the experimental data agrees best with the AMD and CoMD at 300 fm/c for mass, charge, and multiplicity distributions. In the isoscaling analysis, there is a larger asymmetry energy dependence and also a time-step dependence. The experimental data agrees best with the later time-steps and the simulation with GEMINI added. There is a clear trend for the agreement of the experiment with later time-steps in the isoscaling analysis. When using event selections to compare to previous works, the experiment in this work agrees very well with the experiment and conclusions from the previous works. This shows consistency between the experimental data and the simulations. The time-step of the simulation has a large effect on the comparison with experimental data in the isoscaling analysis. Furthermore, in the isoscaling analysis, there is almost no difference in the results when using a dynamical model to de-excite the system and using a statistical model to de-excite the system.

REFERENCES

[1] M. F. Rivet, Ecole Joliot-Curie 2009 Strong interaction in the nuclear medium: new trends., Lacanau : France (2009).

[2] G. R. Choppin, J. O. Liljenzin, and J. Rydberg, Radiochemistry and Nuclear Chemistry. Massachusetts: Butterworth-Heinemann, 2002.

[3] V. Baran, M. Colonna, V. Greco, M. Di Toro, Phys. Rep. 410 335 (2005).

[4] L. W. Chen, C. M. Ko, B. A. Li, G. C. Yong, Front. Phys. China 2 327 (2007).

[5] C. Fuchs, H. H. Wolter, Eur. Phys. J. A 30 5 (2006).

[6] S. Shlomo, V. M. Kolomietz, G. Colò, Eur. Phys. J. A 30 23 (2006).

[7] A. Ono, H. Horiuchi, Prog. Part. Nucl. Phys. 53 501 (2004).

[8] M. Papa, T. Maruyama, A. Bonasera, Phys. Rev. C 64 024612 (2001).

[9] M. Papa, G. Giuliani, A. Bonasera, J. Comp. Phys. 208 403 (2005).

[10] M. Belkacem, V. Latora, A. Bonasera, Phys. Rev. C 52 271 (1995).

[11] V. Giordano, M. Colonna, M. Di Toro, V. Greco, J. Rizzo, Phys. Rev. C 81 044611 (2010).

[12] R. J. Charity, M. A. McMahan, G. J. Wozniak, R. J. McDonald, L. G. Moretto, D. G. Sarantites, L. G. Sobotka, G. Guarino, A. Pantaleo, L. Fiore, A. Gobbi, K. D. Hildenbrand, Nucl. Phys. A 483 371 (1988).

[13] A. S. Botvina, I. N. Mishustin, Eur. Phys. J. A 30 121 (2006)

[14] H. Xi, W. G. Lynch, M. B. Tsang, W. A. Friedman, D. Durand, Phys. Rev. C 59 1567 (1999).

[15] A. Ono, H. Horiuchi, T. Maruyama, A. Ohnishi, Phys. Rev. Lett. 68 2898 (1992).

[16] M. B. Tsang, W. A. Friedman, C. K. Gelbke, W. G. Lynch, G. Verde, H.S. Xu, Phys. Rev. Lett. 86 5023 (2001).

[17] M. B. Tsang, C. K. Gelbke, X. D. Liu, W. G. Lynch, W. P. Tan, G. Verde, H. S. Xu, W. A. Friedman, R. Donangelo, S. R. Souza, C. B. Das, S. Das Gupta, D. Zhabinsky, Phys. Rev. C 64 054615 (2001).

[18] A. Ono, P. Danielewicz, W. A. Friedman, W. G. Lynch, M. B. Tsang, Phys. Rev. C 68 051601 (2003).

[19] S. Wuenschel, R. Dienhoffer, G. A. Souliotis, S. Galanopoulos, Z. Kohley, K. Hagel, D. V. Shetty, K. Huseman, L. W. May, S. N. Soisson, B. C. Stein, A. L. Caraley, S. J. Yennello, Phys. Rev. C 79 061602 (2009).

[20] D. V. Shetty, S. J. Yennello, A. S. Botvina, G. A. Souliotis, M. Jandel, E. Bell, A. Keksis, S. Soisson, B. Stein, J. Iglio, Phys. Rev. C 70 011601 (2004).

[21] D. Henzlova, A. S. Botvina, K-H Schmidt, V. Henzl, P. Napolitani, M. V. Ricciardi, Jour. Phys. G 37 085010 (2010).

[22] G. A. Souliotis, D. V. Shetty, A. Keksis, E. Bell, M. Jandel, M. Veselsky, S. J. Yennello, Phys. Rev. C 73 024606 (2006).

[23] R. Wada, T. Keutgen, K. Hagel, Y. G. Ma, J. Wang, M. Murray, L. Qin, P. Smith, J. B. Natowitz, R. Alfarro, J. Cibor, M. Cinausero, Y. El Masri, D. Fabris, E. Fioretto, A. Keksis, S. Kowalski, M. Lunardon, A. Makeev, N. Marie, E. Martin, Z. Majka, A. Martinez-Davalos, A. Menchaca-Rocha, G. Nebbia, G. Prete, V. Rizzi, A. Ruangma, D. V. Shetty, G. Souliotis, P. Staszel,

M. Veselsky, G. Viesti, E. M. Winchester, S. J. Yennello, W. Zipper, A. Ono, Phys. Rev. C 69 044610 (2004).

[24] Z. Kohley, L. W. May, S. Wuenschel, A. Bonasera, K. Hagel, R. Tripathi, R. Wada, G. A. Souliotis, D. V. Shetty, S. Galanopoulos, M. Mehlman, W. B. Smith, S. N. Soisson, B. C. Stein, S. J. Yennello, Phys. Rev. C 82 064601 (2010).

[25] S. Wuenschel, K. Hagel, R. Wada, J. B. Natowitz, S. J. Yennello, Z. Kohley, C. Bottosso, L. W. May, W. B. Smith, D. V. Shetty, B. C. Stein, S. N. Soisson, G. Prete, Nucl. Inst. Meth. A 604 578 (2009).

[26] M. Murray, R. Wada, T. Keutgen, K. Hagel, Y. G. Ma, J. B. Natowitz, J. Cibor, L. Qin, C. Hamilton, A. Makeev, A. Ono, and the NIMROD Collboration. Progress in Resarch Cyclotron Institute, Texas A&M University, College Station, TX II-15 (2002).

[27] J. C. Steckmeyer, E. Genouin-Duhamel, E. Vient, J. Colin, D. Durand, G. Auger, C. O. Bacri, N. Bellaize, B. Borderie, R. Bougault, B. Bouriquet, R. Brou, P. Buchet, J. L. Charvet, A. Chbihi, D. Cussol, R. Dayras, N. De Cesare, A. Demeyer, D. Doré, J. D. Frankland, E. Galichet, E. Gerlic, D. Guinet, S. Hudan, P. Lautesse, F. Lavaud, J. L. Laville, J. F. Lecolley, C. Leduc, R. Legrain, N. Le Neindre, O. Lopez, M. Louvel, A. M. Maskay, L. Nalpas, J. Normand, M. Pârlog, P. Pawłowski, E. Plagnol, M. F. Rivet, E. Rosato, F. Saint-Laurent, G. Tăbăcaru, B. Tamain, L. Tassan-Got, O. Tirel, K. Turzo, M. Vigilante, C. Volant, J. P. Wieleczko, Nucl. Phys. A 686 537 (2001).